

Banner appropriate to article type will appear here in typeset article

The effects of boundary proximity on Kelvin-Helmholtz instability and turbulence

Chih-Lun Liu¹†, Alexis K. Kaminski², William D. Smyth¹,

¹College of Earth, Ocean and Atmospheric Sciences, Oregon State University, Corvallis, OR 97331.

²Department of Mechanical Engineering, University of California, Berkeley, Berkeley, CA, 94720.

(Received xx; revised xx; accepted xx)

Studies of Kelvin-Helmholtz (KH) instability have typically modelled the initial flow as an isolated shear layer. In geophysical cases, however, the instability often occurs near boundaries and may therefore be influenced by boundary proximity effects. Ensembles of direct numerical simulations are conducted to understand the effect of boundary proximity on the evolution of the instability and the resulting turbulence. Ensemble averages are used to reduce sensitivity to small variations in initial conditions. Both the transition to turbulence and the resulting turbulent mixing are modified when the shear layer is near a boundary: the time scales for the onset of instability and turbulence are longer, and the height of the KH billow is reduced. Subharmonic instability is suppressed by the boundary because phase-lock is prevented due to the diverging phase speeds of the KH and subharmonic modes. In addition, the disruptive influence of three-dimensional secondary instabilities on pairing is more profound as the two events coincide more closely. When the shear layer is far from the boundary, the shear-aligned convective instability is dominant; however, secondary central core instability takes over when the shear layer is close to the boundary, providing an alternate route for the transition to turbulence. Both the efficiency of the resulting mixing and the turbulent diffusivity are dramatically reduced by boundary proximity effects.

1. Introduction

Turbulent mixing plays a crucial role in the vertical exchange of heat, momentum, nutrients, and carbon in the ocean (Wunsch *et al.* 2004). The performance of large-scale ocean and climate models depends on the parameterization of small-scale mixing and turbulent fluxes. Turbulent mixing is often modeled by the classical Kelvin-Helmholtz (KH) instability of a stably-stratified shear layer (e.g. Smyth & Carpenter 2019). The shear layer rolls up to form a periodic train of “billow” structures which subsequently break down via three-dimensional (3D) secondary instabilities (Mashayek & Peltier 2012*a,b*), leading to turbulence and vertical transport.

Turbulence in stratified shear flows has been observed in a variety of fluid environments, ranging from diurnal warm layers near the surface ocean (Hughes *et al.* 2021), equatorial undercurrents (Moum *et al.* 2011), seamounts and oceanic ridges (Chang *et al.* 2016, 2022), estuarine shear zones (Geyer *et al.* 2010; Holleman *et al.* 2016; Tu *et al.* 2022) and the abyssal ocean (Van Haren *et al.* 2014; Van Haren & Gostiaux 2010) to canopy waves

† Email address for correspondence: liuchihl@oregonstate.edu

37 above forests (Mayor 2017, Smyth et al. 2023) and higher atmospheric layers (Fukao *et al.*
 38 2011). Theoretical understanding has been greatly advanced via the use of direct numerical
 39 simulations (Caulfield & Peltier 2000; Mashayek & Peltier 2011, 2012*a,b*; Salehipour *et al.*
 40 2015; Smyth & Moum 2000; Kaminski & Smyth 2019; VanDine *et al.* 2021; Lewin &
 41 Caulfield 2021). However, most theoretical studies have assumed that the shear layer is
 42 located far from any boundary. In geophysical flows, much of the most important mixing is
 43 found in complex boundary regions (Munk & Wunsch 1998; Wunsch *et al.* 2004; Smyth *et al.*
 44 2023); therefore, a comprehensive understanding of boundary effects on sheared, stratified
 45 turbulence is critical for the prediction of such mixing events.

46 This article describes the impact of proximity to a no-slip boundary on KH instability and
 47 its secondary instabilities as well as the resulting turbulent mixing. We seek to understand
 48 how the boundary modifies the route to turbulence and the ensuing turbulence characteristics,
 49 e.g., mixing efficiency. In the process, we identify and explore a novel mechanism for the
 50 suppression of pairing and turbulence by boundary effects.

51 Subharmonic pairing, wherein adjacent KH billows merge (Corcos & Sherman 1976;
 52 Klaassen & Peltier 1989; Smyth & Peltier 1993) leads to upscale energy cascade and may
 53 increase turbulent mixing (Rahmani *et al.* 2014) by raising the available potential energy.
 54 This mechanism is sensitive to the details of the initial conditions. For example, Dong
 55 *et al.* (2019) showed how the initial phase difference between the primary KH and the
 56 subharmonic Fourier components leads to a significant difference in mixing characteristics.
 57 Guha & Rahmani (2019) predicted the strength and pattern of pairing in terms of the initial
 58 asymmetry between consecutive wavelengths of the vertical velocity profile.

59 The 3D secondary instabilities initiate a downscale energy cascade and catalyze the
 60 transition to turbulence (Klaassen & Peltier 1985*a*; Mashayek & Peltier 2012*a,b*). Mashayek
 61 & Peltier (2013) showed that pairing can be suppressed, at high Reynolds number, by the
 62 early emergence of various 3D secondary instabilities. This provides one explanation for the
 63 fact that pairing is observed rarely, if ever, in geophysical flows, (although see Armi & Mayr
 64 2011). Here, we propose an alternative mechanism whereby pairing instability is suppressed
 65 by the boundary.

66 Turbulent mixing in stratified fluids is often parameterized using mixing efficiency, η , a
 67 ratio of the irreversible mixing to the rate at which the kinetic energy is irreversibly lost to
 68 viscosity. A canonical constant value of $\Gamma = \eta/(1 - \eta) = 0.2$ ($\eta = 1/6$), known as the flux
 69 coefficient, is often assumed in the parameterization of the eddy diffusivity, $K_\rho = \Gamma \epsilon'/N^2$
 70 (Osborn 1980), where ϵ' is the viscous dissipation rate of turbulent kinetic energy, and N is
 71 the buoyancy frequency. However, previous studies have shown that mixing efficiency is not
 72 necessarily constant (Gregg *et al.* 2018; Ivey *et al.* 2008; Caulfield 2021). Here, our goal is
 73 to understand the effect of boundary proximity on turbulent mixing and its efficiency.

74 We study these phenomena by comparing statistics from ensembles of DNS in which the
 75 initial state is varied slightly and randomly. This is done using ensembles of direct numerical
 76 simulations (DNS), where initial perturbations are varied due to the sensitive dependence
 77 on initial conditions (Liu *et al.* 2022). Liu *et al.* (2022) showed that a small change in the
 78 initial random perturbation can lead to a substantial variation in the timing and strength of
 79 turbulence. This variation results from the interactions between mean flow, primary KH,
 80 subharmonic, and various 3D secondary instabilities.

81 The paper is organized as follows. In §2 we describe the setup for our numerical simulations
 82 and the choice of the initial parameter values as well as the diagnostic tools required for the
 83 analysis of energetics and mixing. We then describe the boundary effects on primary KH
 84 instability in §3, and show that the evolution of KH instability depends strongly on boundary
 85 proximity. In §4 we explain how the boundary suppresses pairing by altering the phase
 86 speeds of the KH and subharmonic modes. Boundary effects on 3D secondary instabilities are

87 presented in §5. In §5.4, we show how boundary proximity modifies the competition between
 88 the subharmonic instability and turbulence. In §6, we describe the boundary effects on the
 89 irreversible mixing, mixing efficiency and turbulent diffusivity. Conclusions are summarized
 90 in §7.

91 2. Methodology

92

2.1. The mathematical model

93 We begin by considering a stably-stratified parallel shear layer,

$$94 \quad U^*(z) = U_0^* \tanh\left(\frac{z^*}{h^*} + \frac{L_z^*/2 - d^*}{h^*}\right) \quad \text{and} \quad B^*(z) = B_0^* \tanh\left(\frac{z^*}{h^*} + \frac{L_z^*/2 - d^*}{h^*}\right) \quad (2.1)$$

96 in which $2U_0^*$ and $2B_0^*$ are, respectively, velocity and buoyancy differences across the shear
 97 layer and $2h^*$ is its thickness (figure 1). Asterisks indicate dimensional quantities. The
 98 stratified shear layer has a distance d^* from the lower boundary. The domain has a vertical
 99 extent L_z^* . The Cartesian coordinates are x^* (streamwise), y^* (spanwise) and z^* (vertical,
 100 positive upwards). The non-dimensional velocity and buoyancy profiles become:

$$101 \quad U(z) = B(z) = \tanh\left(z + \frac{L_z}{2} - d\right), \quad (2.2)$$

102
 103 after nondimensionalizing velocities by U_0^* , buoyancy by B_0^* , lengths by h^* , and times by the
 104 advective timescale h^*/U_0^* .

105 The flow evolution is governed by the Boussinesq Navier-Stokes equations, conservation
 106 of buoyancy and mass continuity equations. In non-dimensional form, these are:

$$107 \quad \frac{\partial \mathbf{u}}{\partial t} + \mathbf{u} \cdot \nabla \mathbf{u} = -\nabla p + Ri_0 b \hat{z} + \frac{1}{Re_0} \nabla^2 \mathbf{u}, \quad (2.3)$$

$$108 \quad \frac{\partial b}{\partial t} + \mathbf{u} \cdot \nabla b = \frac{1}{Re_0 Pr} \nabla^2 b, \quad (2.4)$$

$$109 \quad \nabla \cdot \mathbf{u} = 0, \quad (2.5)$$

111 where $\mathbf{u} = \{u, v, w\}$ is the net velocity, b is the buoyancy, p is the pressure and \hat{z} is the
 112 vertical unit vector. The equations include three non-dimensional parameters, namely the
 113 initial Reynolds number, $Re_0 = U_0^* h^* / \nu^*$, where ν^* is the kinematic viscosity, the Prandtl
 114 number, $Pr = \nu^* / \kappa^*$, where κ^* is the diffusivity and the initial bulk Richardson number,
 115 $Ri_0 = B_0^* h^* / U_0^{*2}$.

116 In general, the gradient Richardson number is defined by,

$$117 \quad Ri_g = \frac{\partial \langle b^* \rangle_{xy} / \partial z^*}{(\partial \langle u^* \rangle_{xy} / \partial z^*)^2} = Ri_0 \frac{\partial \langle b \rangle_{xy} / \partial z}{(\partial \langle u \rangle_{xy} / \partial z)^2}. \quad (2.6)$$

119 The notation $\langle \rangle_r$ denotes an average over r , where r may represent any combination of x , y ,
 120 z and t . When $t > 0$, the minimum gradient Richardson number over z is named as Ri_{min} . In
 121 the inviscid limit, $Ri_{min} < 1/4$ is a necessary condition for instability (Miles 1961; Howard
 122 1961). For the flow described by (2.2), the initial minimum Ri_g is given by Ri_0 .

123 Boundary conditions are periodic in both horizontal directions. The top boundary is
 124 free-slip ($\partial u / \partial z = \partial v / \partial z = 0$). The bottom boundary is no-slip and moves with velocity
 125 $u = -\tanh(d)$, $v = 0$ (figure 1) so that the speed differential between the mean flow and
 126 the boundary is ~ 0 . The advantage of setting the no-slip boundary as a moving boundary
 127 is that the timestep can be larger based on the Courant–Friedrichs–Lewy condition. Both
 128 boundaries are insulating ($\partial b / \partial z = 0$) and impermeable ($w = 0$).

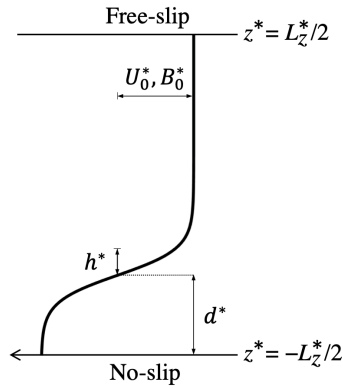


Figure 1: Initial mean profile for buoyancy and velocity showing dimensional parameters and boundary conditions. The bottom boundary moves to the left with speed $-U_0^* \tanh(d^*/h^*)$ for computational efficiency.

129 A small, random velocity perturbation is added to the initial state (2.2). This initial
 130 noise field is purely random and is applied to all three velocity components throughout the
 131 computational domain. The maximum amplitude of any one component is 0.05, or 2.5%
 132 of the velocity change across the shear layer, small enough that the initial growth phase is
 133 described by linear perturbation theory. Ensembles of simulations are performed, each using
 134 a different seed to generate the random velocities (Liu *et al.* 2022). The choices of d , grid
 135 sizes and repetition of runs for each set of simulations are presented in table 1.

136

2.2. Linear Stability Analysis

137 To calculate the linear instabilities, (2.3-2.5) are linearized about the initial base flow (2.2)
 138 and perturbed by small-amplitude, normal mode disturbances proportional to the real part
 139 of $a(z) \exp(\sigma t + ikx)$. Here, $a(z)$ is the vertically-varying, complex amplitude of any
 140 perturbation quantity, σ is a complex exponential growth rate and k is the wavenumber
 141 in the streamwise direction. The phase speed is defined as $c = -\sigma_i/k$, where the subscript
 142 i denotes the imaginary part. The normal mode equations are expressed in matrix form and
 143 discretized using a finite difference method to form a generalized eigenvalue problem (Smyth
 144 & Carpenter 2019).

145

2.3. Direct Numerical Simulations

146 The simulations are carried out using DIABLO (Taylor 2008), which utilizes a mixed implicit-
 147 explicit timestepping scheme with pressure projection method. The viscous and diffusive
 148 terms are handled implicitly with a second-order Crank-Nicolson method; other terms are
 149 treated explicitly with a third-order Runge-Kutta-Wray method. The vertical z direction
 150 dependence is approximated using a second-order finite-difference method, while the periodic
 151 streamwise and spanwise (x , y) directions are handled pseudospectrally.

152 To allow the subharmonic mode to grow, two wavelengths of the fastest growing KH mode
 153 are accommodated in the streamwise periodicity interval L_x based on linear stability analysis
 154 (section 2.2). The spanwise periodicity interval $L_y = L_x/4$ is adequate for the development
 155 of 3D secondary instabilities (e.g. Klaassen & Peltier 1985; Mashayek & Peltier 2013). The
 156 domain height is $L_z = 20$, sufficient to avoid boundary effects for simulations of isolated
 157 shear layer.

158 The computational grid is uniform and isotropic. Grid dimensions are chosen to resolve
 159 ~ 2.5 times the Kolmogorov length scale, $L_k = (Re^{-3}/\epsilon')^{1/4}$ after the onset of turbulence.

160 Due to the sensitive dependence on initial conditions that may greatly alter the evolution
 161 of the instability and turbulent mixing (Liu *et al.* 2022), an adequate ensemble size is
 162 crucial for controlling sampling error. Therefore, we must compromise between Re , Pr , and
 163 ensemble size. Since we are focused mainly on the boundary proximity effect, the initial state
 164 parameters, Richardson, Reynolds, and Prandtl numbers are fixed. We conduct a total of 60
 165 DNS runs, ensembles of 10 cases for different values of d . In all cases, we set $Re_0 = 1000$,
 166 the smallest value at which the suppression of pairing is clearly manifested. We choose
 167 $Ri_0 = 0.12$, large enough for stratification to be important but small enough for pairing to
 168 develop without being entirely damped by stratification. We choose $Pr = 1$, an appropriate
 169 value for air but too small to be entirely realistic in water, a compromise that has to be made
 170 due to computational resource limits.

171 2.4. Diagnostics

The total velocity field can be decomposed into a horizontally-averaged component (the mean flow) and a perturbation (Caulfield & Peltier 2000):

$$\mathbf{u}(x, y, z, t) = \bar{U}\hat{\mathbf{e}}^{(x)} + \mathbf{u}'(x, y, z, t), \quad \text{where } \bar{U}(z, t) = \langle u \rangle_{xy},$$

where $\hat{\mathbf{e}}^{(x)}$ is the unit vector in the streamwise direction. The perturbation velocity is further partitioned into two-dimensional (2D) and three-dimensional (3D) components

$$\mathbf{u}'(x, y, z, t) = \mathbf{u}_{2d} + \mathbf{u}_{3d},$$

where

$$\mathbf{u}_{2d}(x, z, t) = \langle u \rangle_y - \bar{U}\hat{\mathbf{e}}^{(x)}, \quad \text{and } \mathbf{u}_{3d}(x, y, z, t) = \mathbf{u} - \mathbf{u}_{2d} - \bar{U}\hat{\mathbf{e}}^{(x)} = \mathbf{u} - \langle u \rangle_y.$$

The buoyancy field can be decomposed with the same manner as the velocity field, therefore the three-dimensional component can be defined as

$$b_{3d}(x, y, z, t) = b - \langle b \rangle_y.$$

172 Following the decomposition of the velocity, the total kinetic energy can be subdivided as

$$173 \quad \mathcal{K} = \bar{\mathcal{K}} + \mathcal{K}'; \quad \mathcal{K}' = \langle \mathcal{K}_{2d} \rangle_{xz} + \langle \mathcal{K}_{3d} \rangle_{xyz}, \quad (2.7)$$

where

$$\bar{\mathcal{K}} = \frac{1}{2} \left\langle \bar{U}^2 \right\rangle_z, \quad \mathcal{K}_{2d} = \frac{1}{2} (u_{2d}^2 + v_{2d}^2 + w_{2d}^2), \quad \mathcal{K}_{3d} = \frac{1}{2} (u_{3d}^2 + v_{3d}^2 + w_{3d}^2).$$

175 These constituent kinetic energies $\bar{\mathcal{K}}$, \mathcal{K}' , \mathcal{K}_{2d} and \mathcal{K}_{3d} may be identified respectively
 176 as the horizontally averaged kinetic energy associated with the mean flow, the turbulent
 177 kinetic energy, and the kinetic energy associated with two- and three-dimensional motions,
 178 respectively. The time at which $\langle \mathcal{K}_{3d} \rangle_{xyz}$ is maximum is defined as t_{3d} .

179 It is also convenient to partition the kinetic energy into components associated with certain
 180 wavenumbers by Fourier decomposition. The Fourier transform of the perturbation velocity
 181 field at $z = 0$ is

$$182 \quad \hat{\mathbf{u}}'(k, y, t) = \frac{1}{L_x} \int_0^{L_x} \mathbf{u}'(x, y, t) e^{-ikx} dx, \quad (2.8)$$

183 where $k = \frac{2\pi}{L_x}n$, $n = 1, 2, 3, \dots, \frac{N_x}{2} - 1$, and $N_x = 512$ for the array sizes used here. The

184 spectral decomposition of the perturbation kinetic energy is then defined as,

$$185 \quad \widehat{\mathcal{K}}'(k, t) = \frac{1}{2} \left(\langle \widehat{u}' \widehat{u}'^* \rangle_y + \langle \widehat{v}' \widehat{v}'^* \rangle_y + \langle \widehat{w}' \widehat{w}'^* \rangle_y \right), \quad (2.9)$$

186 where \widehat{u}'^* is the complex conjugate of the transformed perturbation velocity component. The
187 turbulent kinetic energy is given by

$$188 \quad \mathcal{K}'(t) = \sum_{n=1}^{\frac{N_x}{2}-1} \widehat{\mathcal{K}}'_n. \quad (2.10)$$

189 We denote the subharmonic component as \mathcal{K}_{sub} for $n = 1$, and the KH component as \mathcal{K}_{KH}
190 for $n = 2$. The time at which \mathcal{K}_{sub} and \mathcal{K}_{KH} are maxima are defined as t_{sub} and t_{KH} ,
191 respectively.

192 We calculate the phase spectrum of the perturbation vertical velocity by taking the Fourier
193 transform of $\langle w' \rangle_y$. The result can then be expressed as

$$194 \quad \widehat{w}'(k, t) = \widehat{W}(k) e^{i\widehat{\phi}(k)}, \quad (2.11)$$

195 where $\widehat{W}(k)$ and $\widehat{\phi}(k)$ are, respectively, the amplitude spectrum and the phase spectrum.

196 A key process that we wish to quantify is the irreversible mixing. To do so, we decompose
197 the total potential energy $\mathcal{P} = -Ri_0 \langle bz \rangle_{xyz}$ into available and background components,
198 $\mathcal{P} = \mathcal{P}_a + \mathcal{P}_b$. \mathcal{P}_b is the minimum potential energy that can be achieved by adiabatically
199 rearranging the buoyancy field into a statically stable state b^* (Winters *et al.* 1995; Tseng
200 & Ferziger 2001). After computing the total and background potential energy, available
201 potential energy is calculated from the residual, $\mathcal{P}_a = \mathcal{P} - \mathcal{P}_b$. \mathcal{P}_a is the potential energy
202 available for conversion to kinetic energy, which arises due to lateral variations in buoyancy
203 or statically unstable regions.

204 Following Caulfield & Peltier (2000), we define the irreversible mixing rate due to fluid
205 motions \mathcal{M} as,

$$206 \quad \mathcal{M} = \frac{d\mathcal{P}_b}{dt} - \mathcal{D}_p. \quad (2.12)$$

208 where $\mathcal{D}_p \equiv Ri_0(b_{top} - b_{bottom})/(RePrL_z)$ denotes the rate at which the potential energy
209 of a statically stable density distribution would increase in the absence of any fluid motion
210 (i.e., due only to diffusion of the mean buoyancy profile).

211 We define the instantaneous mixing efficiency as

$$212 \quad \eta_i = \frac{\mathcal{M}}{\mathcal{M} + \epsilon}, \quad (2.13)$$

214 where we use the total dissipation rate $\epsilon = \frac{2}{Re} \langle s_{ij} s_{ij} \rangle_{xyz}$, and $s_{ij} = (\partial u_i / \partial x_j + \partial u_j / \partial x_i) / 2$
215 is the strain rate tensor. The mixing efficiency relates the fraction of energy that goes into
216 irreversible mixing to the total lost of kinetic energy that is irreversibly lost by the fluid (Peltier
217 & Caulfield 2003). We note that there are a variety of definitions for mixing efficiency in the
218 literature (Gregg *et al.* 2018). A cumulative mixing efficiency is also useful for quantifying
219 the efficiency of the entire mixing event, and is defined as

$$220 \quad \eta_c = \frac{\int_{t_i}^{t_f} \mathcal{M} dt}{\int_{t_i}^{t_f} \mathcal{M} dt + \int_{t_i}^{t_f} \epsilon dt}, \quad (2.14)$$

221 where $t_i \sim 2.2$, is the initial time after the model adjustment period, and t_f is the final time
222 of the simulation at which the TKE drops more than 3 orders of magnitude.

d	(L_x, L_y, L_z)
10	(28.28, 7.07, 20)
6	(28.56, 7.14, 20)
4	(28.21, 7.05, 20)
3	(28.36, 7.09, 20)
2.5	(27.93, 6.98, 20)
2	(29.16, 7.29, 20)

Table 1: Parameter values for six, 10-member DNS ensembles. In all cases $Re_0 = 1000$, $Pr = 1$, $Ri_0 = 0.12$, and the grid size is $512 \times 128 \times 361$. The maximum initial random velocity component is 0.05.

223 The evolution of kinetic energy equation associated with the 3D perturbations can be
 224 expressed in the form (Caulfield & Peltier 2000)

$$225 \quad \sigma_{3d} = \frac{1}{2\langle \mathcal{K}_{3d} \rangle_{xyz}} \frac{d}{dt} \langle \mathcal{K}_{3d} \rangle_{xyz} \quad (2.15)$$

$$226 \quad = \mathcal{R}_{3d} + \mathcal{S}h_{3d} + \mathcal{A}_{3d} + \mathcal{H}_{3d} + \mathcal{D}_{3d}, \quad (2.16)$$

228 where the first two terms represent the 3D perturbation kinetic energy extraction from the
 229 background mean shear and the background 2D KH billow by means of Reynolds stresses,
 230 respectively defined as

$$231 \quad \mathcal{R}_{3d} = -\frac{1}{2\langle \mathcal{K}_{3d} \rangle_{xyz}} \left\langle u_{3d} w_{3d} \frac{\partial \bar{U}}{\partial z} \right\rangle_{xyz}, \quad (2.17)$$

$$232 \quad \mathcal{S}h_{3d} = -\frac{1}{2\langle \mathcal{K}_{3d} \rangle_{xyz}} \left\langle (u_{3d} w_{3d}) \left(\frac{\partial u_{2d}}{\partial z} + \frac{\partial w_{2d}}{\partial x} \right) \right\rangle_{xyz}. \quad (2.18)$$

234 The third term represents the stretching/compression of the 3D vorticity and is defined as

$$235 \quad \mathcal{A}_{3d} = -\frac{1}{2\langle \mathcal{K}_{3d} \rangle_{xyz}} \left\langle \frac{1}{2} (u_{3d}^2 - w_{3d}^2) \left(\frac{\partial u_{2d}}{\partial x} - \frac{\partial w_{2d}}{\partial z} \right) \right\rangle_{xyz}. \quad (2.19)$$

237 The final two terms are the buoyancy production term and the negative-definite viscous
 238 dissipation term associated with 3D perturbations and are defined respectively as

$$239 \quad \mathcal{H}_{3d} = \frac{Ri_0}{2\langle \mathcal{K}_{3d} \rangle_{xyz}} \langle b_{3d} w_{3d} \rangle_{xyz}, \quad (2.20)$$

$$240 \quad \mathcal{D}_{3d} = -\frac{1}{\langle \mathcal{K}_{3d} \rangle_{xyz} Re} \langle s_{ij} s_{ij} \rangle_{xyz}, \quad (2.21)$$

242 where s_{ij} is the strain rate tensor of the 3D motions. There are no additional terms in (2.16)
 243 associated with boundary fluxes, but all terms are ultimately affected by the boundary.

244 3. Overview

245 Consider a tanh shear layer (as in figure 1) with $Ri_{min} < 1/4$ and weak viscosity and diffusion
 246 located far from any boundary (figure 2a). The incipient KH instability grows to macroscopic
 247 amplitude and generates a train of KH billows of which our computational domain contains
 248 two (figure 2b). In the next phase, adjacent billows pair (figure 2c). Thereafter, the billow

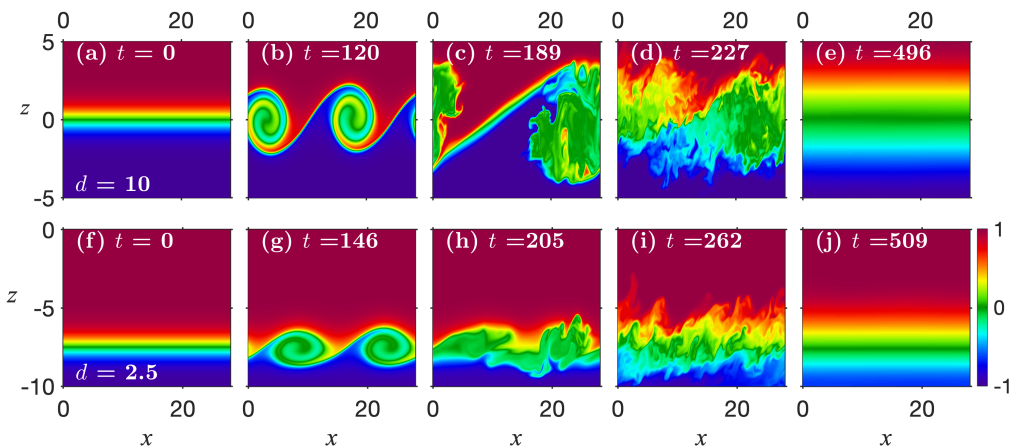


Figure 2: Cross-sections through $y = 0$ at various times for (a – e) shear layer far from boundary ($d = 10$, case #3), (f – j) shear layer close to boundary ($d = 2.5$, case #1). Frames (b) and (g) are at their respective t_{KH} .

249 structure breaks down as 3D secondary instabilities create turbulence (figure 2d). Finally, the
 250 flow relaminarizes. The shear layer is now stable because $Ri_{min} > 1/4$ (figure 2e).

251 When the instability occurs near the boundary ($d = 2.5$; second row of figure 2), the
 252 evolution of the KH instability shares some resemblance with the $d = 10$ cases. The
 253 linear instability grows to finite amplitude (figure 2g), then 3D secondary instabilities arise
 254 and turbulence is generated, breaking down the KH billows (figure 2h,i). Finally, the flow
 255 relaminarizes to a stable state (figure 2j). When $d = 2.5$, the vertical extent of the KH billow
 256 at $t = t_{KH}$ (figure 2g) is 55% of that for $d = 10$ (figure 2b). In other words, KH billows
 257 are flatter when the shear layer is closer to the boundary. (The vertical extent of the billows
 258 is defined as the distance between two local maximum buoyancy gradients at the upper and
 259 lower edges of the billows.) This result is consistent with previous lab experiments (Holt
 260 1998). The geometrical change occurs because the impermeable boundary constrains the
 261 vertical development of the billows.

262 Another impact of the boundary is that the primary KH instability grows slower so the
 263 onset of turbulence is delayed. The maximum \mathcal{K}_{KH} occurs at $t_{KH} = 120$ for $d = 10$ (figure
 264 2b) but is delayed to $t_{KH} = 145$ for $d = 2.5$ (figure 2g). A more robust demonstration of the
 265 boundary effect on the KH evolution is the dependence of t_{KH} on d (figure 3). When the
 266 boundary effect becomes salient, e.g., $d < 4$, t_{KH} increases significantly with decreasing d .

267 4. Pairing

268 In a train of KH billows, there is a range of different wavelengths including the primary KH
 269 wavelength, along with its shorter harmonics and longer subharmonics. Like all interfacial
 270 disturbances, KH instability decays exponentially and vertically away from the interface
 271 (Smyth & Carpenter 2019). The decay depth is proportional to the wavelength. Therefore,
 272 we can expect that the subharmonic mode (twice the wavelength of the fastest-growing KH
 273 mode) is influenced by the boundary most strongly because it has the greatest vertical reach.
 274 In this section, we explore the mechanisms whereby the subharmonic instability is affected
 275 by the boundary.

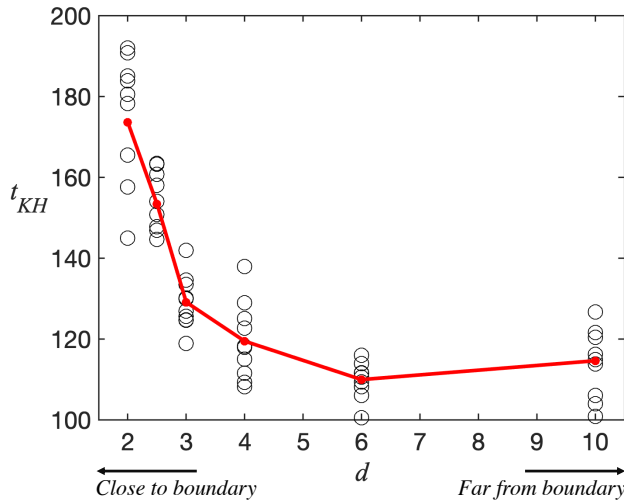


Figure 3: Dependence of t_{KH} on d . Circles denote all ensemble members. Red represents the mean.

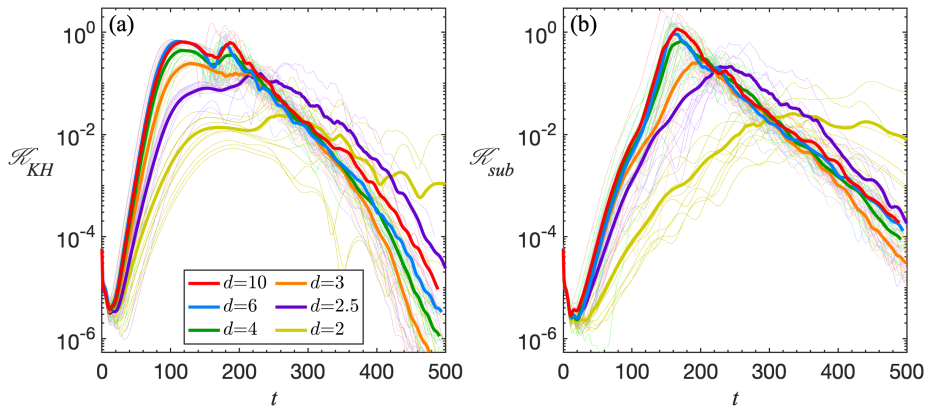


Figure 4: Time variation of kinetic energy of the (a) primary KH and (b) subharmonic Fourier components with different values of d . Each thick curve represents the average of all cases with the same d .

276

4.1. Energy Evolution

277 The evolution of \mathcal{K}_{KH} and \mathcal{K}_{sub} with different values of d is shown in figure 4. The
 278 dependence of these energies on d can be viewed as two distinct regimes. The change of
 279 \mathcal{K}_{KH} and \mathcal{K}_{sub} is slight when $d \geq 4$ (red, blue and green curves are close together), but
 280 precipitous when $d < 4$ (orange, purple and yellow curves are widely separated). We interpret
 281 this to mean that boundary effects become significant when $d < 4$.

282 One possible consequence of subharmonic instability is pairing, which can increase mixing
 283 significantly (Rahmani *et al.* 2014). However, pairing is found mainly in idealized simulations
 284 and laboratory experiments; it is rarely observed in geophysical flows. A possible explanation
 285 is provided by the discovery that, at high Reynolds number, pairing can be suppressed by the

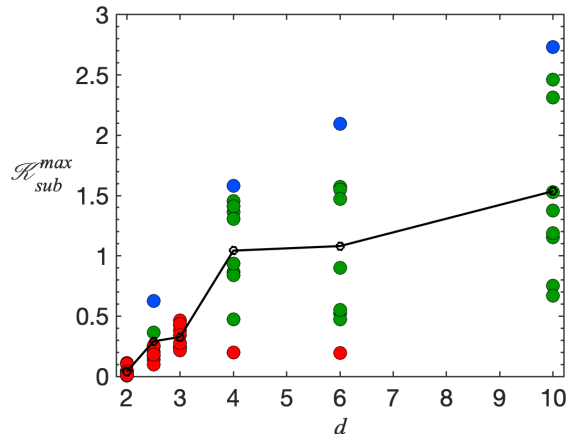


Figure 5: Dependence of maximum subharmonic kinetic energy on d . The ensemble members exhibiting laminar pairing, turbulent pairing, and non-pairing are represented by blue, green, and red circles, respectively, while the mean is indicated by the black line.

286 early emergence of a “zoo” of three-dimensional secondary instabilities (Mashayek & Peltier
 287 2011, 2013, 2012b). Another well-known mechanism that suppresses pairing is background
 288 stratification, which restricts vertical motion, thereby stabilizing the subharmonic mode
 289 whenever Ri_0 exceeds approximately $3/16$ (i.e. instability requires $Ri_0 < k(1 - k)$ and the
 290 subharmonic wavenumber is $k \approx 1/4$, e.g. Smyth & Carpenter 2019, §4.4). In the present
 291 simulations, we ensure that pairing is not prevented by either 3D secondary instability or
 292 stratification by choosing $Re_0 = 1000$ and $Ri_0 = 0.12$ for all cases.

293 Here we propose that the boundary can be another important factor in suppressing pairing.
 294 In the examples shown in figure 2, pairing occurs when $d = 10$ but not when $d = 2.5$. To
 295 generalize the distinction, we examine the ensemble average of many cases (figure 4b and
 296 5) over a range of d values. Similar to the dependence on Re (Mashayek & Peltier (2013)
 297 figure 21), we find that the maximum of \mathcal{K}_{sub} decreases monotonically with decreasing
 298 d . Therefore, the boundary effect has similar influence on pairing to the Reynolds number
 299 effect, although the underlying mechanism is different.

300 The spread of \mathcal{K}_{sub}^{max} tends to be larger when d is large (figure 5). This is because the
 301 pairing process is sensitive to small changes in the initial conditions. Billow evolution can
 302 be categorized as laminar pairing, turbulent pairing or non-pairing (Liu *et al.* 2022; Guha
 303 & Rahmani 2019; Dong *et al.* 2019). Laminar pairing involves the greatest amount of
 304 subharmonic kinetic energy (blue circles in figure 5), because at the time when \mathcal{K}_{sub} is
 305 a maximum, turbulence has not yet grown strong enough to collapse the coherent billow
 306 structure. When the boundary effect is negligible (e.g. when $d = 10$), laminar pairing occurs
 307 in a single case. Other cases with $d = 10$ produce turbulent pairing (green circles), in which
 308 turbulence drains part of the kinetic energy from the emerging paired billow. When the shear
 309 layer is located close to the boundary, the maximum subharmonic kinetic energy decreases.
 310 Furthermore, more cases fail to pair (red circles). Among cases that successfully pair, most
 311 are already turbulent (turbulent pairing, green circles), while laminar pairing becomes less
 312 likely. The spread of \mathcal{K}_{sub}^{max} between cases is usually smaller when d is small.

313 One might expect that the suppression of pairing by the boundary would be accomplished
 314 via damping of the subharmonic KH instability, and such damping is in fact found for $d < 4$
 315 (figure 6, red curve). However, a hint that the mechanism is more subtle than this is revealed
 316 by the growth rate of the primary KH mode, σ_{KH} (figure 6, blue curve), which decreases

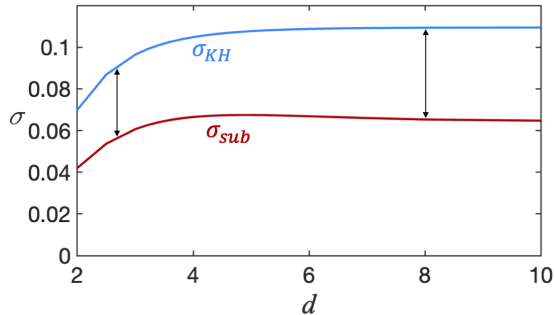


Figure 6: Dependence of KH growth rate and subharmonic growth rate on d from linear stability analysis with $Ri_0 = 0.12$, $Re_0 = 1000$ and $Pr = 1$.

317 even more than does σ_{sub} , i.e. the growth rate of the subharmonic *relative to the primary*
 318 increases. Based only on this comparison of growth rates, one would expect pairing to take
 319 longer but to actually be *more pronounced* at low d , contrary to figure 2. We will describe
 320 the mechanism whereby the boundary effect suppresses pairing in the following subsection.

321 4.2. Phase evolution

322 The optimal separation between the KH and subharmonic modes is,

$$323 \Delta_{sub}^{KH} \equiv \frac{x_{KH} - x_{sub}}{\lambda_{KH}} = \frac{3}{4} + n, \quad (4.1)$$

324 where n is an arbitrary integer, λ_{KH} is the wavelength of the KH mode and x_{KH} and x_{sub}
 325 are the crest positions of the KH and subharmonic vertical velocity profiles, respectively
 326 (figure 7a). These positions are computed from the Fourier phase spectrum of the centerline
 327 vertical velocity. In this configuration, one KH billow is lifted and its neighbour is lowered
 328 by the vertical motion of the subharmonic mode (Figure 7a). Thereafter, the mean shear
 329 feeds energy to the pairing billows, and a single vortex is formed (Dong *et al.* 2019; Guha &
 330 Rahmani 2019). The opposite value of the optimal Δ_{sub}^{KH} is $1/4 + n$ (figure 7b). In this case,
 331 one vortex rotates in the same direction as the subharmonic vorticity, while the other one
 332 rotates oppositely and is thus canceled out. This process is referred to as draining (Klaassen
 333 & Peltier 1989).

334 The evolution of Δ_{sub}^{KH} (Figure 8) shows that the KH and subharmonic modes require some
 335 time to lock on. The onset and end of the lock-on process are ambiguous, especially when
 336 d is small. Nonetheless, the lock-on period can be qualitatively viewed as the period during
 337 which the change of Δ_{sub}^{KH} is the smallest (i.e. the dotted curve is most nearly horizontal).
 338 For $d = 10$ (figure 8a), the lock-on value is $3/4$ from approximately $t \sim 100$ to 150 during
 339 which time pairing occurs. The highlighted red coloured case locks on to the pairing position
 340 $\Delta_{sub}^{KH} = 3/4$ relatively early, $t \sim 100$. The corresponding buoyancy field is shown in the
 341 background of figure 7a, in which laminar pairing can be seen. In the paired state (e.g.
 342 $t = 170$), when billows are replaced by a single vortex, Δ_{sub}^{KH} switches to $1/4$. After the
 343 flow becomes turbulent, Δ_{sub}^{KH} fluctuates chaotically because the billows break down into
 344 turbulence, therefore Δ_{sub}^{KH} is not meaningful.

345 In cases with lower d , several changes complicate the lock-on process: (1) Δ_{sub}^{KH} changes

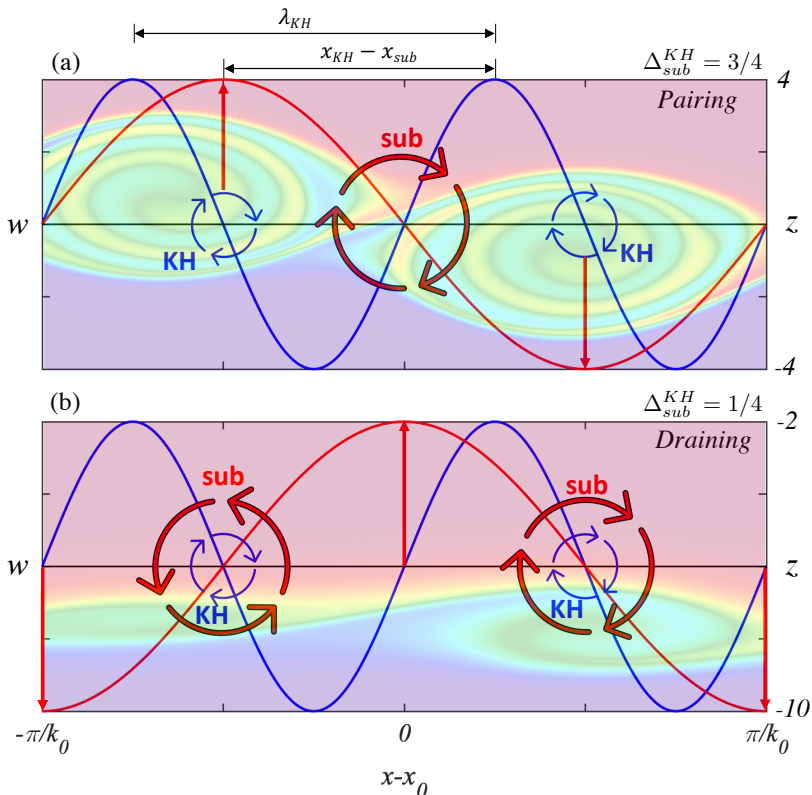


Figure 7: Schematic of vorticity and vertical motions in terms of the subharmonic and KH modes at the onset of (a) pairing instability with optimal $\Delta_{sub}^{KH} = 3/4$ ($d = 10$, case #7) and (b) draining instability with optimal $\Delta_{sub}^{KH} = 1/4$ ($d = 2.5$, case #2). Buoyancy snapshots in the background of both panels demonstrate the corresponding structure. k_0 is the subharmonic wavenumber and x_0 is a midway point between billows.

346 in time more rapidly, (2) the time during which phase-locking is sustained decreases, and (3)
 347 the value of Δ_{sub}^{KH} at which phase-locking occurs departs from 3/4, eventually approaching
 348 1/4 (Figure 8b-e). For $d = 6$, the lock-on value is slightly larger than 3/4 during $t \sim 110$
 349 to 150 (figure 8b); for $d = 4$, the lock-on value is $\sim 7/8$ during $t \sim 120 - 150$ (figure 8c), and
 350 for $d = 3$, the lock-on value increases to ~ 1 or equivalently 0 (i.e. x_{KH} and x_{sub} at the same
 351 position) during $t \sim 150$ to 170 (figure 8d). When $d = 2.5$ (figure 8e), the lock-on value
 352 becomes less clear because the time variation of Δ_{sub}^{KH} increases. Nonetheless, we can still
 353 roughly estimate the lock-on value by determining the time at which most cases converge
 354 to a similar Δ_{sub}^{KH} value. With this approach, a reasonable lock-on value is 1/4 at $t \sim 170$
 355 (figure 8e), which coincides with the optimal value for draining. The buoyancy field of the
 356 red-highlighted case, in which one vortex is enhanced while the other is suppressed, is shown
 357 in the background of figure 7b. This result does not imply that draining always occurs when
 358 $d = 2.5$; draining can often be absent depending on the details of the initial conditions (Liu
 359 *et al.* 2022).

360 It is not a coincidence that the draining lock-on value for the case $d = 2.5$ and the paired
 361 state lock-on value for the case $d = 10$ (e.g. $t = 150$) are both $\Delta_{sub}^{KH} \simeq 1/4$. This is because
 362 the pairing and draining mechanisms, though very different, both transform a pair of billows

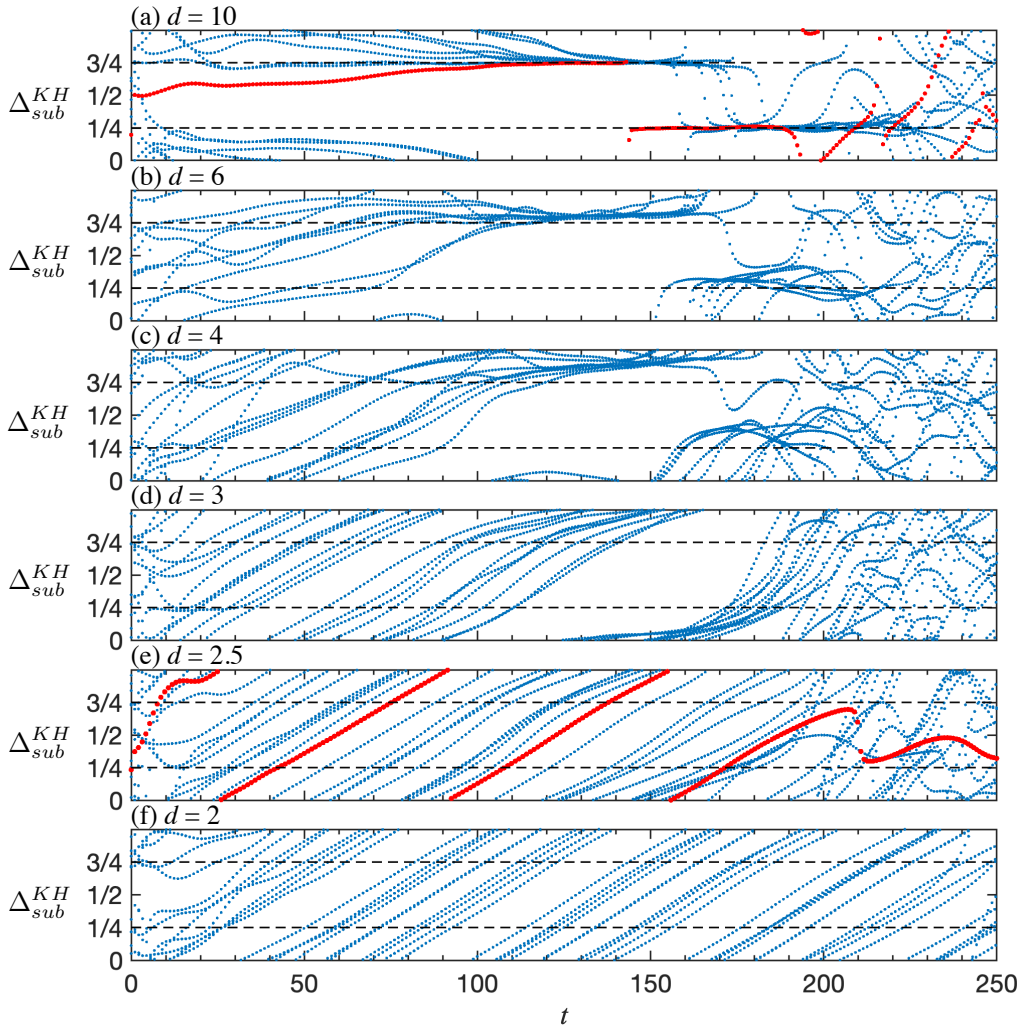


Figure 8: Time variations of Δ_{sub}^{KH} with different values of d . Two horizontal dashed lines in each panel denote the optimal lock-on value, $\Delta_{sub}^{KH} = 3/4$, and the opposite of optimal value, $\Delta_{sub}^{KH} = 1/4$, respectively. Red curves indicate the cases selected in figure 7.

363 into a single vortex. When d is even smaller ($d = 2$), the lock-on value and period are highly
 364 ambiguous. The boundary effect prevents the KH and subharmonic phases from locking on
 365 altogether, and therefore pairing is suppressed.

366 The phase difference Δ_{sub}^{KH} at $t = 0$ exhibits substantial variability in all cases; however,
 367 this variability diminishes considerably during phase locking. This indicates that the phase-
 368 locking value is not significantly contingent upon the initial random noise. When the boundary
 369 effect is prominent, significant variability is evident between simulations from the beginning
 370 to the end.

371 For the small- d cases (figure 8e,f), the steady, rapid increase of Δ_{sub}^{KH} suggests an ongoing
 372 change in the phase speeds of the KH and subharmonic modes. This is confirmed by linear
 373 stability analysis (figure 9). The fastest-growing KH instability has a phase speed c_{KH} while
 374 its subharmonic has half the KH wavenumber by definition, and the phase speed is c_{sub} .

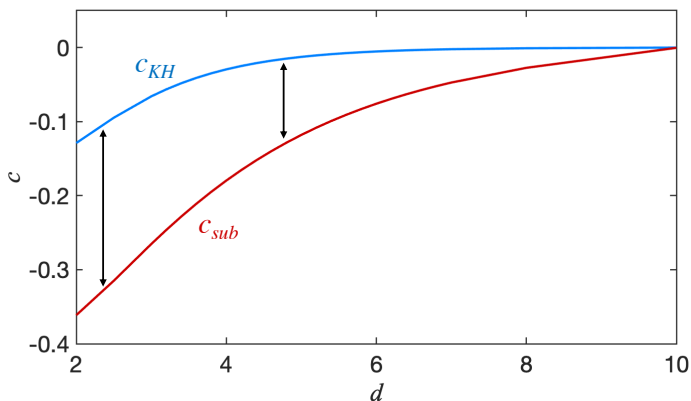


Figure 9: Dependence of KH phase speed and subharmonic phase speed on d from linear stability analysis with $Ri_0 = 0.12$, $Re = 1000$ and $Pr = 1$.

375 When the boundary effects are negligible ($d = 10$), both c_{KH} and c_{sub} are ~ 0 . However,
 376 when the shear layer is closer to the boundary, the phase speeds diverge. Therefore, x_{KH} and
 377 x_{sub} are constantly changing, which explains the constant change of Δ_{sub}^{KH} seen in figure 8b-f.
 378 Thus, boundary proximity impedes phase-locking of the KH and subharmonic modes by
 379 causing their phase speeds to diverge. In extreme cases of small d (figure 8f), phase-locking
 380 and pairing are prevented altogether.

381 The dependence of the phase speed difference between the KH and subharmonic modes
 382 on the parameters Re_0 , Pr and Ri_0 is also of interest as a step toward a broader exploration
 383 of the parameter space. KH instabilities change very little with increasing Re_0 once Re_0
 384 exceeds $\sim O(10^2)$ (Smyth et al. 2013); hence, we see little dependence of the phase speed
 385 difference $c_{KH} - c_{sub}$ (figure 10a). The same is true of the Prandtl number (figure 10b).
 386 There is a slight dependence on Ri_0 (figure 10c) when d is small: the contour (thick contour)
 387 corresponding to the phase speed difference found at $Ri_0 = 0.12$, $d = 4$ varies between
 388 $d = 3.7$ at very low Ri_0 and $d = 4.6$ at high Ri_0 . Therefore the threshold $d \sim 4$ for the
 389 suppression of phase-locking (and thus pairing) by boundary effects may vary only weakly
 390 with Ri_0 . Further DNS is needed to explore the dependence of boundary effects on these
 391 parameters in the nonlinear regime.

392 5. Three-dimensional Secondary Instabilities

393 Three-dimensional secondary instabilities catalyze the transition to turbulence, which in
 394 turn leads to irreversible mixing. Various 3D secondary instabilities have been discovered;
 395 notably, the shear-aligned convective instability (Davis & Peltier 1979; Klaassen & Peltier
 396 1985) appears when KH billows become large enough to overturn the buoyancy gradient.
 397 Herein, we focus on some of the instabilities that help to explain the sources and sinks of 3D
 398 perturbation kinetic energy in shear layers centered at different distances from the boundary.
 399 We begin by examining the case $d = 10$, where boundary effects are negligible (§5.1). We
 400 then examine differences that arise when $d = 2.5$ (§5.2) and boundary effects are dominant.

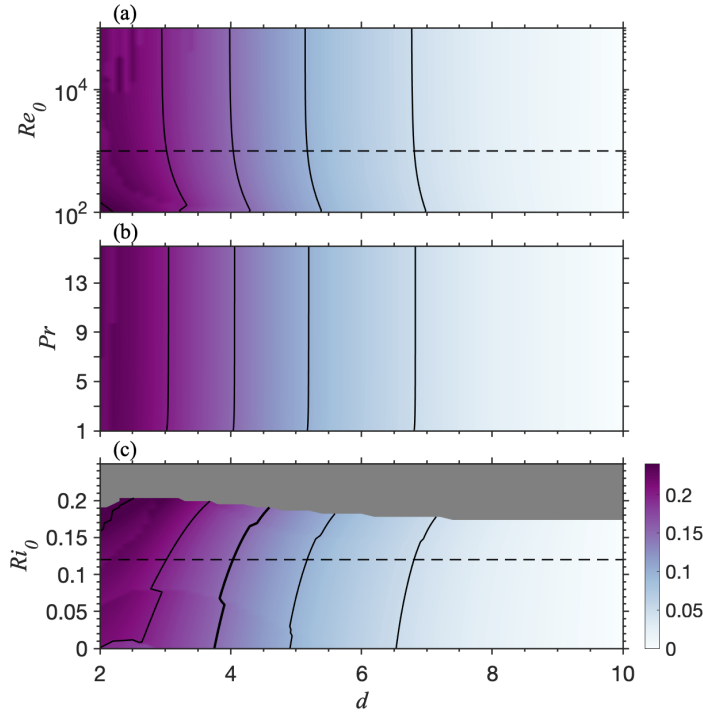


Figure 10: Phase speed difference between unstable KH and subharmonic modes. A nonzero phase speed difference indicates that the KH and subharmonic modes phase lock only if forced to do so by nonlinear effects. (a) relationship between d and Re_0 at a fixed value of $Ri_0 = 0.12$ and $Pr = 1$. (b) relationship between d and Pr at a fixed value of $Ri_0 = 0.12$ and $Re_0 = 1000$. (c) relationship between d and Ri_0 at $Re_0 = 1000$ and $Pr = 1$. The growth rate in the shaded region of (c) is below the cutoff value, 0.001. Black contours represent phase speed difference with an interval of 0.05. Horizontal dashed lines indicate $Re_0 = 1000$ and $Ri_0 = 0.12$, respectively, in (a) and (c).

401

5.1. $d = 10$: Negligible boundary effects

402 Three-dimensional secondary instabilities grow mostly between $t \sim 90$ and $t \sim 180$ (figure
 403 11a, blue curve). This growth starts after the saturation of the primary KH instability, when
 404 $\langle \mathcal{K}_{2d} \rangle_{xz}$ starts to decline (red curve). Two times, indicated by the diamonds in figure 11a,
 405 have been selected to illustrate the form of the 3D motions in terms of the spanwise-averaged
 406 \mathcal{H}_{3d} . The first of these represents the early growth of $\langle \mathcal{H}_{3d} \rangle_y$ ($t = 108$, figure 11c), the
 407 second the time of most rapid growth ($t = 136$).

408 The form of the 3D motions changes because the KH billow develops different 3D
 409 instabilities as its geometry evolves. We therefore focus on the 3D perturbation kinetic
 410 energy evolution to explain the changes. In the early stage ($0 < t < 90$), there is no 3D
 411 instability. Growth is negative due mostly to viscous dissipation of the initial noise field.

412 During the earliest stage of 3D growth, represented by time $t = 108$ (first diamond in
 413 figure 11b), 3D motions are concentrated in the cores of the KH billows (figure 11c) and the
 414 \mathcal{H}_{3d} budget is dominated by the shear production term \mathcal{R}_{3d} (figure 11b). This is because the
 415 spanwise vortex tube at the core of each billow is distorted sinusoidally. Spanwise vorticity
 416 is thus redirected towards the $x - z$ plane such that the Reynolds stress $\langle u_{3d} w_{3d} \rangle_{xyz}$ becomes
 417 negative (as illustrated in Smyth 2006, figure 8). This 3D stress field works with the mean
 418 shear $d\bar{U}/dz$ to produce 3D kinetic energy. Since $d\bar{U}/dz$ is large near the billow core, the
 419 shear production quantified by \mathcal{R}_{3d} is dominant. This 3D secondary instability exhibits

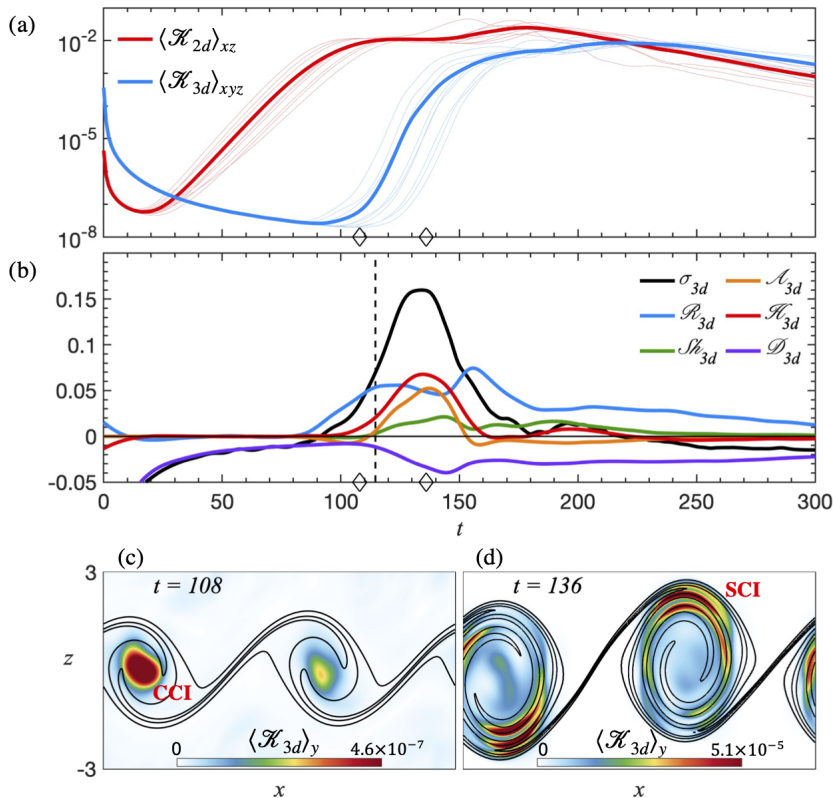


Figure 11: Negligible boundary effect when $d = 10$. (a) Time variation of two-dimensional and three-dimensional volume-averaged kinetic energy. The thick line is ensemble-averaged and thin lines represent all cases. (b) Time variation of different terms of the σ_{3d} evolution equation (2.16). All terms are ensemble-averaged. Vertical dashed lines represent ensemble averaged t_{KH} . For clarity in plotting, lower resolution time series have been interpolated to higher temporal resolution using cubic splines. (c) and (d) show spanwise-averaged \mathcal{H}_{3d} for $d = 10$, case #3 at $t = 108$ and $t = 136$, respectively. The contour lines represent spanwise-averaged buoyancy with an interval of 0.4. Note that the colour scales for (c) and (d) are different. Times correspond to the diamond symbols in (a) and (b).

420 similar characteristics to the central core mode found in Klaassen & Peltier (1991), hence
 421 we identify it as central-core instability (CCI).

422 During the maximum growth stage ($t = 136$, second diamond in figure 11b), 3D motions
 423 in the central core are no longer dominant as $\langle \mathcal{H}_{3d} \rangle_y$ is mainly concentrated at the margins
 424 of the billows (figure 11d). At this stage, the primary KH billows roll up. This results in
 425 regions of statically unstable buoyancy variation within and surrounding the billow cores.
 426 The buoyancy production \mathcal{H}_{3d} becomes the dominant energy source while \mathcal{A}_{3d} and $\mathcal{S}_{h_{3d}}$
 427 also increase. This is all consistent with the emergence of shear-aligned convection rolls via
 428 the secondary convective instability (SCI; Klaassen & Peltier 1985a). Vorticity is created
 429 when vortex tubes are stretched and is exchanged between different components when vortex
 430 tubes bend and tilt. The 2D velocity gradients increase along with the stretching and bending
 431 of vortex tubes surrounding the billows, the stretching deformation term, \mathcal{A}_{3d} , and the shear
 432 deformation term, $\mathcal{S}_{h_{3d}}$, both increase.

433 Beyond the time when σ_{3d} is a maximum, the billows start to pair at $t \sim 150$, and \mathcal{R}_{3d}
 434 regains its dominance over the other terms. The shear-aligned convection rolls are still active
 435 at the periphery of the billow core, but gradually break down into turbulence; therefore
 436 \mathcal{H}_{3d} declines toward zero. After the pairs of billows have amalgamated, the extraction of
 437 3D perturbation kinetic energy from the background mean shear decreases. During the
 438 post-turbulent stage, all terms gradually decay.

439 The fact that the evolution of \mathcal{R}_{3d} when boundary effects are negligible includes two local
 440 maxima is consistent with the findings of Mashayek & Peltier (2013). However, they found
 441 that, prior to billow saturation, buoyancy production is the major source term while we found
 442 that \mathcal{R}_{3d} is dominant. The difference may be due to a difference in the initial random noise
 443 field — Mashayek & Peltier (2013) applied noise to both the buoyancy and velocity fields
 444 whereas we perturbed only the velocity.

445 5.2. $d = 2.5$: Strong boundary effects

446 When the boundary effect is strong (e.g. $d = 2.5$), growth rates of both $\langle \mathcal{K}_{2d} \rangle_{xz}$ and $\langle \mathcal{K}_{3d} \rangle_{xyz}$
 447 are reduced relative to cases with negligible boundary effects (compare figures 11a and 12a),
 448 as are their maximum values.

449 At maximum growth ($t = 176$, figure 12d), there are neither clear unstable sublayers nor
 450 3D motions in layers surrounding the billows. Instead, $\langle \mathcal{K}_{3d} \rangle_y$ remains concentrated in the
 451 core, suggesting that SCI is suppressed. A conspicuous impact of the boundary is that \mathcal{R}_{3d}
 452 dominates all other source terms from the initial-growth stage of the instability to the post-
 453 turbulent stage (figure 12b), rather than being supplanted by \mathcal{H}_{3d} as the primary billows roll
 454 up (cf. §5.1). The buoyancy production term \mathcal{H}_{3d} (red line in figure 12b), \mathcal{A}_{3d} , and $\mathcal{S}h_{3d}$ are
 455 small throughout the evolution because the overturning within the billow is suppressed by
 456 the boundary. This suggests that the balance is mostly between the energy extraction from
 457 the background mean shear and the viscous dissipation of the 3D perturbations.

458 We conclude that three-dimensionalization is via CCI alone when the boundary effect is
 459 strong (figures 12c and 12d).

460 5.3. Effects of boundary proximity on secondary convective instability

461 We have seen that, for the single case $d = 2.5$, the main effect of the boundary on 3D
 462 instabilities is the suppression of SCI. The Rayleigh number provides a compact metric for
 463 SCI that we can examine as a function of d , thus gaining a more comprehensive view of the
 464 boundary proximity effect. We define the Rayleigh number at t_{KH} for the statically unstable
 465 regions (Klaassen & Peltier 1985) as:

$$466 \quad Ra = -Re^2 Ri_0 Pr \frac{\partial \bar{b}}{\partial z} \delta^4, \quad (5.1)$$

467 where $\frac{\partial \bar{b}}{\partial z}$ is the average buoyancy gradient across the most unstable layer, and δ is its
 468 dimensionless thickness. The critical Ra for convective instability in a layer with free-slip
 469 upper and lower boundaries, an approximation to the superadiabatic regions found here, is
 470 $Ra_c \approx 657.5$ (e.g. Smyth & Carpenter 2019).

471 When $d \geq 4$ (figure 13), Ra is more than 1 order of magnitude larger than Ra_c , suggesting
 472 that SCI is prominent. A precipitous drop in Ra can be seen when $d < 4$, indicating that
 473 the boundary suppresses SCI (as seen in figure 12). Most cases for $d = 2$ fail to satisfy the
 474 criterion $Ra > Ra_c$, and as a result, convective motions are suppressed within the KH billow.

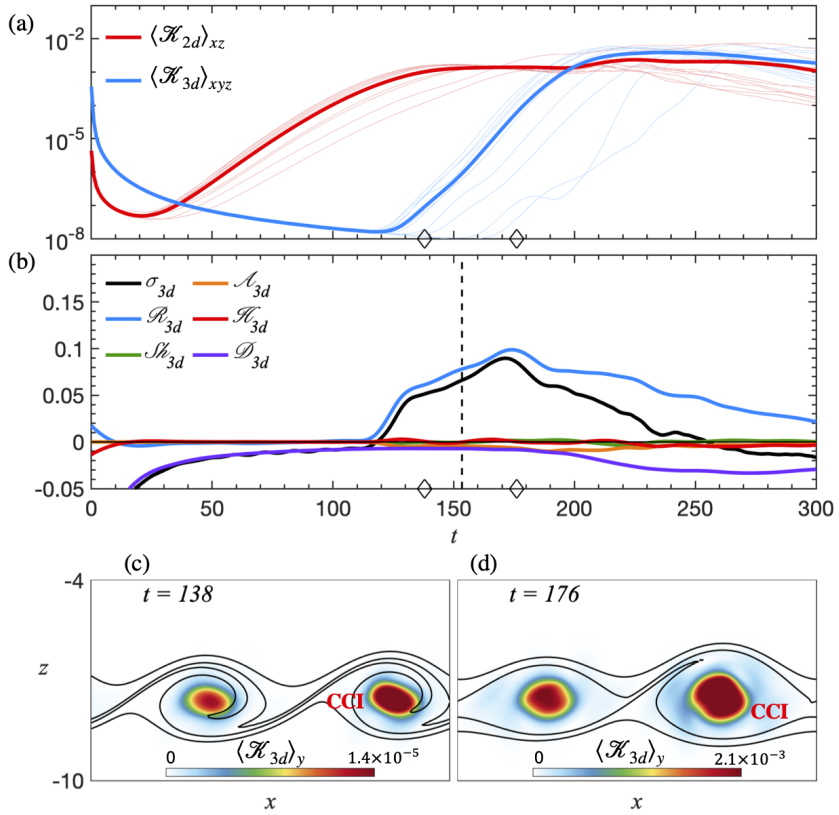


Figure 12: Similar to figure 11 but with the case $d = 2.5$. Case #1 is selected for (c) and (d).

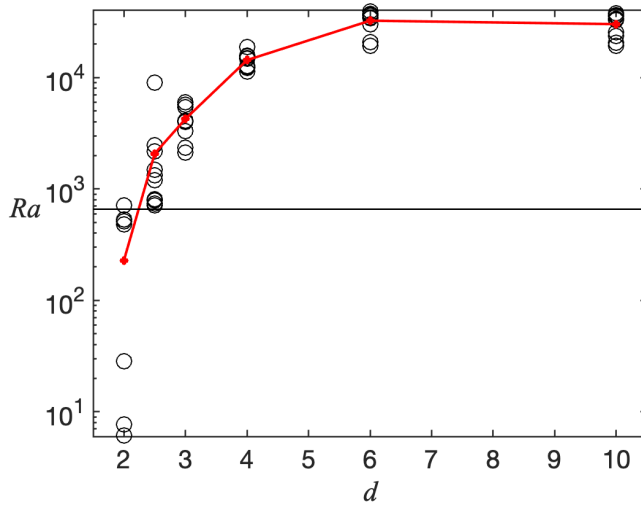


Figure 13: Dependence of Rayleigh number on d at t_{KH} . Circle symbols are all ensemble cases and red dots indicate the mean of the ensembles. Horizontal line denotes the critical Rayleigh number Ra_c , and has a value of 657.5.

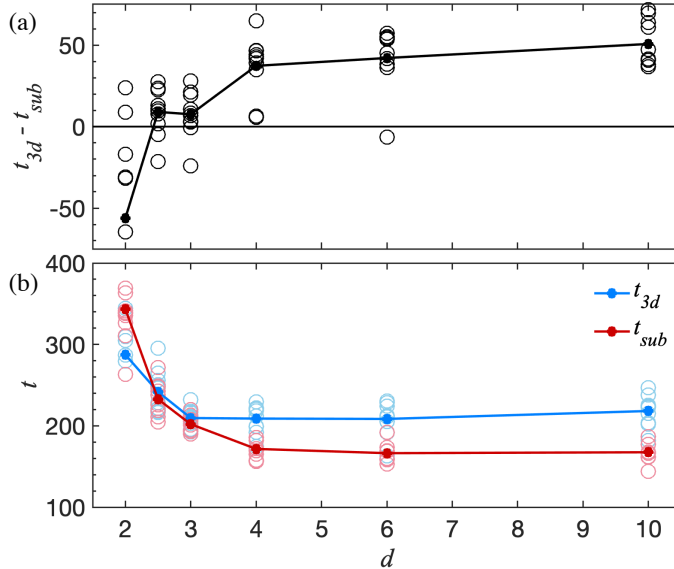


Figure 14: (a) Dependence of time difference between t_{3d} and t_{sub} on d . (b) Dependence of t_{3d} and t_{sub} on d . Circles are all ensemble cases. Data points represent the ensemble mean. The deviated cases of $d = 2$ are not shown in the figure.

475

5.4. Timing of subharmonic and 3D secondary instabilities

476

477

478

479

480

481

482

483

484

485

486

487

488

489

490

491

492

493

494

The timing of the turbulence emergence relative to the subharmonic instability is critical to pairing (Mashayek & Peltier 2013; Liu *et al.* 2022) and therefore to mixing. Thus, t_{sub} and t_{3d} are useful measures for understanding the competition between the subharmonic and 3D secondary instabilities. The difference between t_{3d} and t_{sub} tends to decrease as d decreases (figure 14a). This suggests that the subharmonic instability is more susceptible to interference by turbulence when the boundary effect is strong. (The slope of the mean $t_{3d} - t_{sub}$ versus d is reversed between $d = 2.5$ and $d = 3$, but the reversal is not statistically significant.)

To identify the source of this behaviour, we next focus on t_{sub} and t_{3d} individually (figure 14b). A monotonic increase of t_{sub} with decreasing d can be seen (figure 14b); the increase becomes more pronounced when $d < 4$. Thus, \mathcal{K}_{sub} requires more time to reach to its maximum when the boundary effect is greater. The increase of t_{sub} is owing to the fact that phase lock between the KH and subharmonic modes is prevented due to the divergence of the corresponding phase speeds (§4).

The increase of t_{3d} with decreasing d when $d < 4$ is due to suppression of 3D secondary instabilities by the boundary, as has been demonstrated in §5.2. Even though t_{sub} increases considerably at $d = 2$ and $d = 2.5$, 3D secondary instabilities (and hence the onset of turbulence) are also delayed. Therefore, subharmonic instability may arise at $d = 2.5$ because turbulence emerges too late to overtake it. When $d = 2$, the subharmonic does not reach maximum amplitude until after 3D secondary instabilities have already appeared.

495

6. Turbulent Mixing

496

497

498

In the latter part of each simulation, the flow consists of slowly decaying sheared turbulence. The energy in the 3d motions is supported mainly by shear production (figures 11b and 12b, blue curves) and diminished by viscosity (purple curves). We now discuss the energy budget

499 of this turbulence in the context of irreversible mixing. The instantaneous mixing efficiency
 500 has been calculated using (2.13) and is shown in figure 15c, as are the irreversible mixing
 501 rate (figure 15a) and the total dissipation rate (figure 15b) for various boundary proximity
 502 values. Initially, a large dissipation rate arises due mainly to the viscous decay of the random
 503 noise. Dissipation rapidly decreases to a near-constant (though nonzero) value as the mean
 504 flow continues to diffuse (figure 15b), while the mixing rate is near zero.

505 For all d , the instantaneous mixing rate \mathcal{M} and mixing efficiency exhibit two peaks (figure
 506 15a and c). The first peak of \mathcal{M} and η_i (e.g. at $t \sim 130$, $d = 10$) is associated with the roll-up of
 507 the KH billows. Because they are not yet turbulent, the KH billows develop strong buoyancy
 508 gradients where \mathcal{M} is large. During this time, \mathcal{P}_a is rapidly converted to background potential
 509 energy \mathcal{P}_b (figure 15d and 15e). The dissipation rate is smaller than the mixing rate because
 510 the flow is not turbulent at this stage; hence the irreversible mixing efficiency η_i is greatest.

511 When the shear layer is close to the boundary (small d), the roll-up of the KH billows
 512 weakens, and SCI (§5.2) is therefore suppressed. Because of this, the first peak of \mathcal{M} (e.g.
 513 red curve at $t = 140$ when $d = 3$ in figure 15a) is reduced. Boundary proximity also reduces
 514 dissipation during this time (figure 15b).

515 A precipitous drop in η_i occurs immediately after the first local maximum (figure 15c), due
 516 to the emergence of the 3D secondary instabilities that collapse the KH billows. $\langle \mathcal{K}_{3d} \rangle_{xyz}$
 517 rapidly increases at this stage, e.g. $t \sim 140 - 160$ for $d = 10$ (figure 15g), suggesting
 518 the emergence of 3D turbulence. Therefore, \mathcal{P}_a (figure 15d) as well as $\langle \mathcal{K}_{2d} \rangle_{xz}$ (figure
 519 15f) drop to a local minimum because the 2D KH billow structure is partly destroyed.
 520 As a consequence, the instantaneous mixing efficiency decreases as \mathcal{M} is reduced but ϵ
 521 simultaneously increases.

522 The second peak of \mathcal{M} and η_i (e.g. at $t \sim 200$ for $d = 10$ in figure 15a) is associated
 523 with the turbulent stage of the flow evolution. The dissipation rate (figure 15b) reaches its
 524 maximum shortly after the maximum of \mathcal{M} . Pairing involves significant vertical motion and
 525 thus enhances \mathcal{P}_a (e.g. $t = 150 - 180$ when $d = 10$ in figure 15d). Therefore, \mathcal{P}_b and \mathcal{M}
 526 both increase at $t = 180$. In contrast, the suppression of pairing by the boundary effect (e.g.
 527 $t = 200$ when $d = 3$ in figure 15d) reduces \mathcal{P}_a as well as \mathcal{P}_b . As a result, mixing efficiency
 528 is reduced.

529 During the fully turbulent stage, the instantaneous mixing efficiency roughly converges
 530 to the canonical value of $\eta_i \sim 1/6$ or $\Gamma = 0.2$. In the post-turbulent stage, \mathcal{M} drops to ~ 0
 531 whereas the mean kinetic energy continues to dissipate. Therefore, η_i gradually decays to
 532 ~ 0 .

533 We further relate the mixing efficiency to a turbulent diffusivity associated with irreversible
 534 mixing devised by (Salehipour & Peltier 2015, their equation 2.23). Using the present
 535 nondimensionalization, this is

$$536 \quad K_\rho = \Gamma \frac{Re_b}{Re_0}, \quad (6.1)$$

537 where Re_b is the buoyancy Reynolds number $\epsilon^*/\nu^* N^{*2}$. The time variation of K_ρ is shown in
 538 figure 15h with different values of d . The first peak of K_ρ is associated with the roll up of the
 539 KH billow, during which the mixing efficiency is maximum. The second peak is associated
 540 with turbulence, where ϵ and $\langle \mathcal{K}_{3d} \rangle_{xyz}$ are large. K_ρ drops significantly with decreasing d
 541 as does the mixing rate.

542 We further demonstrate the importance of the route to turbulent mixing by showing the
 543 cumulative mixing, dissipation and mixing efficiency (2.14) for various values of d in figure
 544 16. All three quantities decrease monotonically with decreasing d . The net mixing and
 545 dissipation vary slightly when $d \geq 4$, but drop sharply as $d < 4$ (figure 16a,b). This suggests
 546 that the impact of the boundary on mixing and dissipation becomes prominent when d is
 547

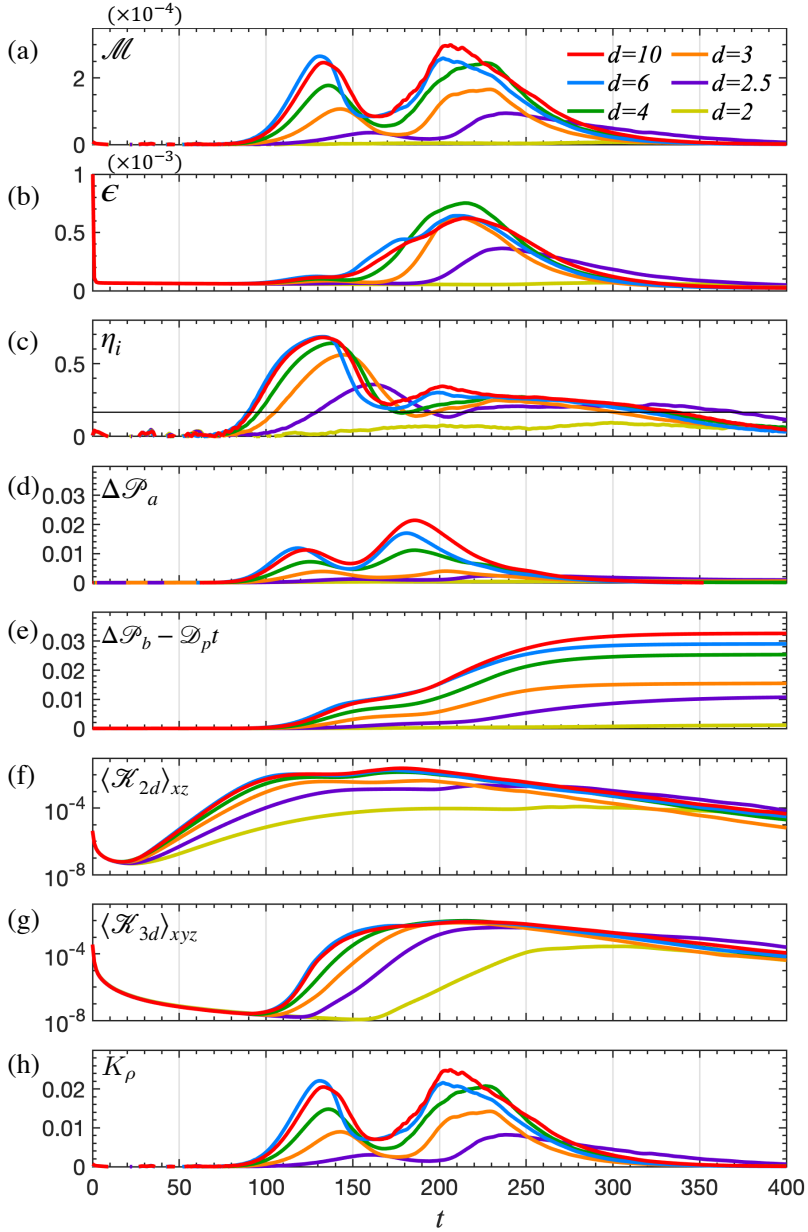


Figure 15: Time variation of (a) mixing rate, (b) total dissipation rate, and (c) instantaneous mixing efficiency with different values of d . Horizontal line denotes the canonical value of $\eta_i \sim 1/6$. Time variation of changes from the initial state in (d) available potential energy \mathcal{P}_a , (e) background potential energy \mathcal{P}_b associated with macroscopic motions. Volume-averaged (f) 2D kinetic energy \mathcal{K}_{2d} , (g) 3D kinetic energy \mathcal{K}_{3d} , (h) Turbulent diffusivity, K_ρ . All curves are ensemble-averaged.

548 less than 4 due to the suppression of pairing and SCI. The abrupt decrease in cumulative
 549 mixing efficiency observed at $d < 4$ could be attributed to a combination of changes in net
 550 dissipation and mixing. We consider the derivative of the cumulative mixing efficiency with

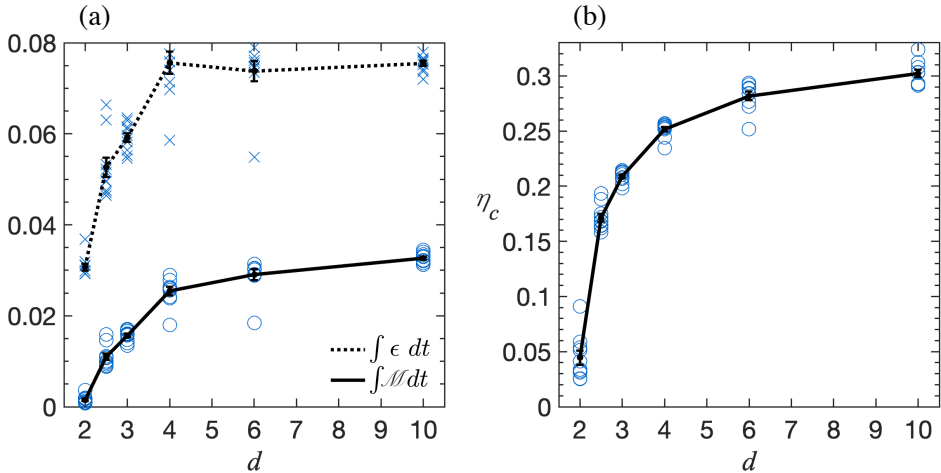


Figure 16: Cumulative (a) mixing (solid line) and dissipation (dotted line), and (b) mixing efficiencies calculated over an entire mixing event for different values of d . Error bars are standard error of the mean.

551 respect to d :

$$552 \quad \frac{1}{\eta_c} \frac{\partial \eta_c}{\partial d} = \frac{1}{\Gamma_c + 1} \left(\frac{1}{\mathcal{M}_c} \frac{\partial \mathcal{M}_c}{\partial d} - \frac{1}{\epsilon_c} \frac{\partial \epsilon_c}{\partial d} \right), \quad (6.2)$$

553 where the subscript “c” refers to cumulative values. The boundary effect diminishes net
 554 dissipation (figure 16a, dotted line), leading to an increase in cumulative mixing efficiency
 555 (6.2, second term in parentheses). However, it also diminishes net mixing, which is a key
 556 factor contributing to the sharp reduction in cumulative mixing efficiency when d is less
 557 than 4. Because the relative change in \mathcal{M}_c is considerably greater than that in ϵ_c , i.e.
 558 $\frac{1}{\mathcal{M}_c} \frac{\partial \mathcal{M}_c}{\partial d} > \frac{1}{\epsilon_c} \frac{\partial \epsilon_c}{\partial d}$, the change in η_c is particularly pronounced.

559 For smaller d , e.g. $d = 2$, the net mixing $\int \mathcal{M} dt$ is small, but the net dissipation persists
 560 since the dissipation of the mean flow is nonzero. Therefore, the efficiency of mixing is
 561 considerably reduced.

562 7. Summary and Discussion

563 In geophysical flow, much of the most important shear-driven turbulent mixing appears
 564 near boundaries. Here, we have shown that boundary proximity significantly modifies the
 565 life cycle of turbulence in a stably-stratified shear layer. A classical KH instability has been
 566 investigated by performing ensembles of DNS experiments with $Re_0 = 1000$, $Ri_0 = 0.12$ and
 567 $Pr = 1$. Absent boundary effects, the moderately low Ri_0 and Re_0 ensure the amalgamation
 568 of the KH billows. Our study describes the impact of boundary proximity on the primary KH
 569 instability, the subharmonic pairing instability, the 3D secondary instability, and the resulting
 570 turbulent mixing.

571 When the shear layer is close to the boundary, the primary KH billows are geometrically
 572 flatter. Furthermore, the evolution of the KH instability is extended over longer periods of
 573 time, so the transition to turbulence is delayed.

574 Mashayek & Peltier (2013) explained that when Re_0 is sufficiently large, the early emerging
 575 3D secondary instabilities can suppress pairing. Pairing would also be suppressed by gravity

576 at higher Ri_0 (Mashayek & Peltier 2012a; Smyth 2003), and tends to be either unchanged or
 577 suppressed with an increase in Pr (Salehipour *et al.* 2015; Rahmani *et al.* 2016). Our study
 578 provides an additional explanation as to why pairing is rarely observed in geophysical flows.
 579 When the boundary effect is negligible, the linear phase speeds of the KH and subharmonic
 580 modes are virtually identical and equal to zero. When the shear layer is close to the boundary,
 581 on the other hand, the KH and subharmonic phase speeds diverge so that phase locking is
 582 prevented and pairing is therefore suppressed.

583 During the time when the primary KH instability is growing exponentially, central-core
 584 instability (CCI) triggers 3D motions in the cores of the billows. This is because the vortex at
 585 the central core tilts, resulting in energy extraction from the background shear via Reynolds
 586 stress. At this stage, CCI dominates for all boundary proximities.

587 When the boundary effect is negligible, secondary convective instability (SCI) becomes
 588 the dominant 3D secondary instability. The buoyancy production is greatly enhanced because
 589 unstable sublayers are formed within the billows. The boundary effect suppresses SCI because
 590 the roll-up of the billows is counteracted by bottom drag. In contrast to the suppression of
 591 SCI, CCI remains dominant throughout the preturbulent stage. By forcing an alternate route
 592 for the transition of a 2D KH billow to 3D turbulence, the boundary effect inevitably changes
 593 the resulting mixing.

594 The suppression of pairing weakens the conversion from \mathcal{P}_a to \mathcal{P}_b and reduces irreversible
 595 mixing. Although the suppression of pairing leads to a decline in dissipation, it is likely that
 596 dissipation near the boundary is amplified when d is smaller. Therefore, instantaneous mixing
 597 efficiency is reduced. Furthermore, the suppression of SCI by the boundary also diminishes
 598 the mixing rate and mixing efficiency. The cumulative irreversible mixing, dissipation and
 599 mixing efficiency, as well as turbulent diffusivity, decrease monotonically with decreasing
 600 distance from the shear layer to the boundary.

601 This study has been confined to a small subset of the continuum of initial states for
 602 practical reasons. Experiments with large Re_0 and Pr are expected to be affected by the
 603 boundary but the effect may manifest differently because the route to turbulent mixing is
 604 inherently different. Both the threshold value for d at which boundary effects become strong
 605 and the onset time of 3D secondary instability are expected to be sensitive to the value of the
 606 Reynolds number. As mentioned in §4, Mashayek & Peltier (2013) show that 3D secondary
 607 instability grows more rapidly when Re_0 is large, therefore, t_{3d} is expected to be smaller and
 608 pairing is, therefore, less likely. The effects of increasing Re_0 on t_{sub} and on the threshold
 609 value of d are subjects for future study.

610 The cores of the KH billows are referred to as “quiet” in observations of the high- Re_0 and
 611 high- Pr flow of a salt-stratified estuary by Geyer *et al.* (2010). DNS experiments have shown
 612 that with large Re_0 and Pr , there is no density variance in the core of the billows but only
 613 in the periphery and the braid (Salehipour *et al.* 2015). This is potentially because the core
 614 of the billows is already well-mixed due to previous 3D secondary instability. In contrast,
 615 our results show that pairing and CCI play an important role during the evolution of the KH
 616 instability and the resulting mixing. A comprehensive understanding of the boundary effects
 617 on shear instability and the resulting turbulent mixing, particularly in the geophysical cases,
 618 will require the exploration of large Re_0 and Pr cases.

619 We have considered a classical KH instability to understand the boundary proximity
 620 effect. However, KH is not the only instability that may arise in a stratified shear flow.
 621 When buoyancy gradients are sufficiently sharp, the flow may be susceptible to the Holmboe
 622 instability (Holmboe 1962). Furthermore, flows with asymmetric background profiles may
 623 exhibit instabilities with a mixture of KH- and Holmboe-like behaviour (e.g. Carpenter *et al.*
 624 2007; Yang *et al.* 2019; Olsthoorn *et al.* 2023). Understanding how boundary proximity
 625 affects these processes may provide insights on future parameterizations of mixing in the

626 ocean near boundaries. Studying beyond shear-driven turbulence and whether the alternative
627 mechanisms have similar mixing properties may also be of future interest.

628 We note that the flow profiles considered here differ from real-world boundary layer flows in
629 two key ways. The first is our choice of a hyperbolic-tangent shear and stratification. Classical
630 turbulent boundary layer flows often exhibit logarithmic profiles with elevated shear at the
631 boundary (e.g. Marusic *et al.* 2013; Bluteau *et al.* 2018), though the specific details of the flow
632 vary with surface roughness, ambient stratification, and external pressure gradients. While
633 the profiles considered here differ from these classical boundary layers, we make this choice
634 so as to facilitate comparison between our simulations and the isolated hyperbolic-tangent
635 shear layer commonly studied in the KH literature. Secondly, the bottom boundary layer or
636 the surface layer in the ocean are often turbulent. While the effect of boundary proximity on
637 KH instability is pronounced, preexisting turbulence should be taken into account for KH
638 instabilities (Brucker & Sarkar 2007; Kaminski & Smyth 2019), especially near boundaries,
639 where mixed layers are not initially laminar.

640 The flat bottom boundary is a simplification, as the real-world topography can be much
641 more complex. Shear instability may occur near a ridge or a sloping topography. Internal
642 waves may be generated near those boundaries, where the base flow may be altered and the
643 boundary effect is not uniform. A nearby surface boundary, e.g. where the shear is created
644 by wind stress in a diurnal warm layer (Hughes *et al.* 2021), can similarly reduce the growth
645 rate of the instability. However, the frictional effect on the shear instability is smaller at the
646 surface than at the bottom, as represented in our model by the free-slip top boundary (§2.1).
647 We have shown that SCI is suppressed by a no-slip boundary because the boundary drag
648 counteracts the roll-up of the billows. Nonetheless, the no-slip condition results in higher
649 dissipation near the boundary, potentially altering the evolution of the billows (Baglaenko
650 2016). With a free-slip boundary, however, no drag counteracts the roll-up process. Therefore,
651 the suppression of SCI due to the free-slip boundary is expected to be smaller. The effects of
652 different boundary types (e.g. free-slip, free-surface) should be a focus for future research.

653 This study can potentially provide insights into future measurements near boundaries in
654 the atmosphere and oceans. The dependence of mixing efficiency on boundary proximity can
655 be estimated via microstructure measurements. Furthermore, acoustic backscatter measure-
656 ments can delineate how the geometry of the KH billows varies with boundary proximity
657 (e.g. Holleman *et al.* 2016; Tu *et al.* 2020).

658 While pairing is rarely detected in geophysical flows, the related phenomena called “tubes”
659 and “knots” are commonly observed in the atmosphere (Thorpe 2002; Smyth & Moum 2012;
660 Fritts *et al.* 2022). Tubes and knots arise when KH billow cores are misaligned. Unlike pairing
661 in our study, knots often appear locally in the spanwise direction. Fritts *et al.* (2022) has
662 found that the transition to turbulence is accelerated and turbulence is significantly stronger in
663 tubes and knots than in other types of secondary instabilities (e.g. SCI). Future studies should
664 address the effects of boundary proximity on tubes and knots. In particular, the question of
665 whether boundary proximity suppresses tubes and knots by reducing the misalignment of
666 the KH billow cores will be of interest.

667 **Acknowledgements.** This paper is part of the first author’s Ph.D. thesis at Oregon State University. We
668 appreciate useful input from advisory committee members Jim Moum, Jim Liburdy, Jonathan Nash and
669 Brodie Pearson. We appreciate John Taylor’s work in creating and curating DIABLO. We acknowledge
670 high-performance computing support on Cheyenne (doi:10.5065/D6RX99HX) provided by NCAR’s Com-
671 putational and Information Systems Laboratory, sponsored by the U.S. National Science Foundation.

672 **Funding.** This work was funded by the US National Science Foundation under grant OCE-1830071. AKK
673 was supported as the Ho-Shang and Mei-Li Lee Faculty Fellow in Mechanical Engineering at UC Berkeley.

674 **Declaration of interests.** The authors report no conflict of interest.

675 **Data availability statement.** DIABLO is available at <https://github.com/johnryantaylor/DIABLO>. Output
676 data is available by request to the authors

677 **Author ORCIDs.** C.-L. Liu, <https://orcid.org/0000-0001-5134-7993>; A. K. Kaminski, <https://orcid.org/0000-0002-4838-2453>; W. D. Smyth, <https://orcid.org/0000-0001-5505-2009>.
678

REFERENCES

- 679 ARMI, LAURENCE & MAYR, GEORG J 2011 The descending stratified flow and internal hydraulic jump in the
680 lee of the Sierras. *Journal of applied meteorology and climatology* **50** (10), 1995–2011.
- 681 BAGLAENKO, ANTON 2016 The effects of confinement on Kelvin-Helmholtz billows. Ph.D. thesis, University
682 of Waterloo, Canada.
- 683 BLUTEAU, C. E., IVEY, G. N., DONIS, D. & MCGINNIS, D. F. 2018 Determining near-bottom fluxes of passive
684 tracers in aquatic environments. *Geophysical Research Letters* **45** (6), 2716–2725.
- 685 BRUCKER, K. & SARKAR, S. 2007 Evolution of an initially turbulent stratified shear layer. *Phys. Fluids* **19**,
686 105105.
- 687 CARPENTER, J.R., LAWRENCE, G.A. & SMYTH, W. D. 2007 Evolution and mixing of asymmetric Holmboe
688 instabilities. *J. Fluid Mech.* **582**, 103–132.
- 689 CAULFIELD, C.P. 2021 Layering, instabilities, and mixing in turbulent stratified flows. *Ann. Rev. Fluid Mech.*
690 **53** (1), 113–145.
- 691 CAULFIELD, C.P. & PELTIER, W.R. 2000 Anatomy of the mixing transition in homogeneous and stratified
692 free shear layers. *J. Fluid Mech.* **413**, 1–47.
- 693 CHANG, MING-HUEI, CHENG, YU-HSIN, YEH, YU-YU, YANG, YIING JANG, JAN, SEN, LIU, CHIH-LUN,
694 MATSUNO, TAKESHI, ENDOH, TAKAHIRO, TSUTSUMI, EISUKE, CHEN, JIA-LIN & OTHERS 2022 Internal
695 hydraulic transition and turbulent mixing observed in the kuroshio over the i-lan ridge off northeastern
696 taiwan. *Journal of Physical Oceanography* **1** (aop).
- 697 CHANG, MING-HUEI, JHENG, SIN-YA & LIEN, REN-CHIEH 2016 Trains of large kelvin-helmholtz billows
698 observed in the kuroshio above a seamount. *Geophysical Research Letters* **43** (16), 8654–8661.
- 699 CORCOS, G.M. & SHERMAN, F.S. 1976 Vorticity concentration and the dynamics of unstable free shear
700 layers. *J. Fluid Mech.* **73**, 241–264.
- 701 DAVIS, P.A. & PELTIER, W.R. 1979 Some characteristics of the Kelvin-Helmholtz and resonant overreflection
702 modes of shear flow instability and of their interaction through vortex pairing. *J. Atmos. Sci.* **36** (12),
703 2394 – 2412.
- 704 DONG, W., TEDFORD, E.W., RAHMANI, M. & LAWRENCE, G.A. 2019 Sensitivity of vortex pairing and mixing
705 to initial perturbations in stratified shear flows. *Phys. Rev. Fluids* **4**, 063902.
- 706 FRITTS, DAVID C, WANG, L, LUND, TS & THORPE, SA 2022 Multi-scale dynamics of kelvin-helmholtz
707 instabilities. part 1. secondary instabilities and the dynamics of tubes and knots. *Journal of Fluid*
708 *Mechanics* **941**.
- 709 FUKAO, SHOICHIRO, LUCE, HUBERT, MEGA, TOMOAKI & YAMAMOTO, MASAYUKI K. 2011 Extensive studies
710 of large-amplitude Kelvin–Helmholtz billows in the lower atmosphere with VHF middle and upper
711 atmosphere radar. *Quarterly Journal of the Royal Meteorological Society* **137** (657), 1019–1041,
712 arXiv: <https://rmetsonline.wiley.com/doi/pdf/10.1002/qj.807>.
- 713 GEYER, W.R., LAVERY, A., SCULLY, M.E. & TROWBRIDGE, J.H. 2010 Mixing by shear instability at high
714 Reynolds number. *Geophys. Res. Lett.* **37**, L22607.
- 715 GREGG, M.C., D’ASARO, E.A., RILEY, J.J. & KUNZE, E. 2018 Mixing efficiency in the ocean. *Ann. Rev.*
716 *Marine Sci.* **10** (1), 443–473.
- 717 GUHA, ANIRBAN & RAHMANI, MONA 2019 Predicting vortex merging and ensuing turbulence characteristics
718 in shear layers from initial conditions. *Journal of Fluid Mechanics* **878**.
- 719 HOLLEMAN, R.C., GEYER, W.R. & RALSTON, D.K. 2016 Stratified turbulence and mixing efficiency in a salt
720 wedge estuary. *J. Phys. Oceanogr.* **46**, 1769–1783.
- 721 HOLMBOE, J. 1962 On the behaviour of symmetric waves in stratified shear layers. *Geophys. Publ.* **24**,
722 67–113.
- 723 HOLT, J. T. 1998 Experiments on kelvin-helmholtz billows influenced by boundaries. *Geophysical &*
724 *Astrophysical Fluid Dynamics* **89** (3-4), 205–233.
- 725 HOWARD, L.N. 1961 Note on a paper of John W. Miles. *J. Fluid Mech.* **10**, 509–512.
- 726 HUGHES, KENNETH G, MOUM, JAMES N, SHROYER, EMILY L & SMYTH, WILLIAM D 2021 Stratified shear
727 instabilities in diurnal warm layers. *Journal of Physical Oceanography* **51** (8), 2583–2598.

- 728 IVEY, G.N., WINTERS, K.B. & KOSEFF, J.R. 2008 Density stratification, turbulence, but how much mixing?
729 *Annu. Rev. Fluid Mech.* **40** (1), 169–184.
- 730 KAMINSKI, A. K. & SMYTH, W. D. 2019 Stratified shear instability in a field of pre-existing turbulence. *J.*
731 *Fluid Mech.* **863**, 639–658.
- 732 KLAASSEN, G.P. & PELTIER, W.R. 1985 The onset of turbulence in finite-amplitude Kelvin-Helmholtz billows.
733 *J. Fluid Mech.* **155**, 1–35.
- 734 KLAASSEN, G.P. & PELTIER, W.R. 1985a The evolution of finite-amplitude Kelvin-Helmholtz billows in two
735 spatial dimensions. *J. Atmos. Sci.* **42**, 1321–1339.
- 736 KLAASSEN, G.P. & PELTIER, W.R. 1989 The role of transverse secondary instabilities in the evolution of free
737 shear layers. *J. Fluid Mech.* **202**, 367–402.
- 738 KLAASSEN, G.P. & PELTIER, W.R. 1991 The influence of stratification on secondary instability in free shear
739 layers. *J. Fluid Mech.* **227**, 71–106.
- 740 LEWIN, S. F. & CAULFIELD, C. P. 2021 The influence of far-field stratification on turbulent mixing. *J. Fluid*
741 *Mech.* **928**, A20.
- 742 LIU, CHIH-LUN, KAMINSKI, ALEXIS K & SMYTH, WILLIAM D 2022 The butterfly effect and the transition to
743 turbulence in a stratified shear layer. *Journal of Fluid Mechanics* **953**, A43.
- 744 MARUSIC, I., MONTY, J. P., HULTMARK, M. & SMITS, A. J. 2013 On the logarithmic region in wall turbulence.
745 *Journal of Fluid Mechanics* **716**, R3.
- 746 MASHAYEK, A. & PELTIER, W. R. 2011 Three-dimensionalization of the stratified mixing layer at high
747 Reynolds number. *Phys. Fluids* **23** (11), 111701, arXiv: <https://doi.org/10.1063/1.3651269>.
- 748 MASHAYEK, A. & PELTIER, W. R. 2012a The ‘zoo’ of secondary instabilities precursory to stratified shear
749 flow transition. Part 1 shear aligned convection, pairing, and braid instabilities. *J. Fluid Mech.* **708**,
750 5–44.
- 751 MASHAYEK, A. & PELTIER, W. R. 2012b The ‘zoo’ of secondary instabilities precursory to stratified shear
752 flow transition. Part 2 the influence of stratification. *J. Fluid Mech.* **708**, 45–70.
- 753 MASHAYEK, A. & PELTIER, W. R. 2013 Shear-induced mixing in geophysical flows: does the route to
754 turbulence matter to its efficiency? *J. Fluid Mech.* **725**, 216–261.
- 755 MAYOR, SHANE D. 2017 Observations of microscale internal gravity waves in very stable atmospheric
756 boundary layers over an orchard canopy. *Ag. Forest Met.* **244-245**, 136 – 150.
- 757 MILES, J.W. 1961 On the stability of heterogeneous shear flows. *J. Fluid Mech.* **10**, 496–508.
- 758 MOUM, J. N., NASH, J. D. & SMYTH, W. D. 2011 Narrowband, high-frequency oscillations in the upper
759 equatorial ocean: Part 1: Interpretation as shear instabilities. *J. Phys. Oceanogr.* **41**, 397–411.
- 760 MUNK, W.H. & WUNCH, C. 1998 Abyssal recipes II: Energetics of tidal and wind mixing. *Deep Sea Res.*
761 **45**, 1977–2010.
- 762 OLSTHOORN, JASON, KAMINSKI, ALEXIS K & ROBB, DANIEL M 2023 Dynamics of asymmetric stratified
763 shear instabilities. *Physical Review Fluids* **8** (2), 024501.
- 764 OSBORN, THOMAS R. 1980 Estimates of the local rate of vertical diffusion from dissipation measurements.
765 *J. Phys. Oceanogr.* **10**, 83–89.
- 766 PELTIER, W.R. & CAULFIELD, C.P. 2003 Mixing efficiency in stratified shear flows. *Annu. Rev. Fluid Mech.*
767 **35**, 136–167.
- 768 RAHMANI, M, LAWRENCE, GA & SEYMOUR, BR 2014 The effect of reynolds number on mixing in kelvin-
769 helmholtz billows. *Journal of fluid mechanics* **759**, 612–641.
- 770 RAHMANI, MONA, SEYMOUR, BR & LAWRENCE, GA 2016 The effect of prandtl number on mixing in low
771 reynolds number kelvin-helmholtz billows. *Physics of Fluids* **28** (5), 054107.
- 772 SALEHIPOUR, H. & PELTIER, W.R. 2015 Diapycnal diffusivity, turbulent Prandtl number and mixing efficiency
773 in Boussinesq stratified turbulence. *J. Fluid Mech.* **775**, 464–500.
- 774 SALEHIPOUR, H., PELTIER, W.R. & MASHAYEK, A. 2015 Turbulent diapycnal mixing in stratified shear flows:
775 the influence of Prandtl number on mixing efficiency and transition at high Reynolds number. *J.*
776 *Fluid Mech.* **773**, 178–223.
- 777 SMYTH, W.D., MAYOR, S.D. & LIAN, Q. 2023 The role of ambient turbulence in canopy wave generation by
778 Kelvin-Helmholtz instability. *Boundary Layer Met.* <https://doi.org/10.1007/s10546-022-00765-y>.
- 779 SMYTH, W. D. 2003 Secondary Kelvin-Helmholtz instability in a weakly stratified shear flow. *J. Fluid Mech.*
780 **497**, 67–98.
- 781 SMYTH, W. D. 2006 Secondary circulations in Holmboe waves. *Phys. Fluids* **18**, 06414.
- 782 SMYTH, W. D. & CARPENTER, J.R. 2019 *Instability in Geophysical Flows*. Cambridge, UK: Cambridge
783 University Press.

- 784 SMYTH, W. D. & MOUM, J. N. 2000 Length scales of turbulence in stably stratified mixing layers. *Phys.*
785 *Fluids* **12**, 1327–1342.
- 786 SMYTH, W. D. & MOUM, J. N. 2012 Ocean mixing by Kelvin-Helmholtz instability. *Oceanography* **5**,
787 140–149.
- 788 SMYTH, W. D. & PELTIER, W. R. 1993 Two-dimensional turbulence in homogeneous and stratified shear
789 layers. *Geophys. Astrophys. Fluid Dyn.* **69**, 1–32.
- 790 TAYLOR, JOHN R 2008 *Numerical simulations of the stratified oceanic bottom boundary layer*. University of
791 California, San Diego.
- 792 THORPE, S.A. 2002 The axial coherence of Kelvin-Helmholtz billows. *Quart. J. Roy. Meteor. Soc.* **128**,
793 1529–1542.
- 794 TSENG, YU-HENG & FERZIGER, JOEL H 2001 Mixing and available potential energy in stratified flows. *Physics*
795 *of Fluids* **13** (5), 1281–1293.
- 796 TU, J., FAN, D., LIAN, Q., LIU, Z., LIU, W., KAMINSKI, A. & SMYTH, W. 2020 Acoustic observations
797 of Kelvin-Helmholtz billows on an estuarine lutocline. *Journal of Geophysical Research: Oceans*
798 **125** (4), e2019JC015383.
- 799 TU, JUNBIAO, FAN, DAIDU, LIU, ZHIYU & SMYTH, WILLIAM 2022 Scaling the mixing efficiency of sediment-
800 stratified turbulence. *Geophysical Research Letters* **49** (13), e2022GL099025.
- 801 VAN HAREN, H. & GOSTIAUX, L. 2010 A deep-ocean Kelvin-Helmholtz billow train. *Geophys. Res. Lett.* **37**,
802 L03605, doi:10.1029/2009GL041890.
- 803 VAN HAREN, H., GOSTIAUX, L., MOROZOV, E. & TARAKANOV, R. 2014 Extremely long Kelvin-Helmholtz
804 billow trains in the Romanche Fracture Zone. *Geophys. Res. Lett.* **41**, 8445–8451.
- 805 VANDINE, ALEXANDRA, PHAM, HIEU T. & SARKAR, SUTANU 2021 Turbulent shear layers in a uniformly
806 stratified background: DNS at high Reynolds number. *J. Fluid Mech.* **916**, A42.
- 807 WINTERS, K., LOMBARD, P.N., RILEY, J.J. & D'ASARO, E. A. 1995 Available potential energy and mixing in
808 density-stratified fluids. *J. Fluid Mech.* **289**, 115–128.
- 809 WUNSCH, CARL, FERRARI, RAFFAELE & OTHERS 2004 Vertical mixing, energy, and the general circulation of
810 the oceans. *Annual Review of Fluid Mechanics* **36** (1), 281–314.
- 811 YANG, ADAM JK, TEDFORD, EW & LAWRENCE, GA 2019 The spatial evolution of velocity and density
812 profiles in an arrested salt wedge. *Theoretical and Applied Mechanics Letters* **9** (6), 403–408.